

# Steady low Reynolds number flow of a generalized Newtonian fluid through a slender elastic tube

Vishal Anand<sup>1</sup> and Ivan C. Christov<sup>1†</sup>

<sup>1</sup>School of Mechanical Engineering, Purdue University, West Lafayette, Indiana 47907, USA

(Received xx; revised xx; accepted xx)

Microfluidic devices are often manufactured using soft polymeric materials, while biological tissues are elastic. Consequently, both can deform significantly due to adjacent fluid flow, even at vanishing Reynolds number (no fluid inertia). Deformation leads to significant enhancement of throughput due to the change in cross-sectional area. The latter engenders a variable pressure gradient in the flow-wise direction and, hence, a nonlinear flow rate–pressure drop relation (unlike the Hagen–Poiseuille law for a rigid tube). To capture non-Newtonian effects of biofluids, we employ the power-law rheological model. The structural problem is reduced to transverse loading of linearly-elastic cylindrical shells. A perturbative approach (in the slenderness parameter) yields analytical solutions for both the flow and the deformation. Specifically, using matched asymptotics, we obtain a uniformly valid solution, which features both a boundary layer and a corner layer, for the coupled flow–deformation problem in a thin, slender deformable microtube. Consequently, we obtain a “generalized Hagen–Poiseuille law” for soft microtubes. We benchmark the mathematical predictions against three-dimensional two-way coupled direct numerical simulations (DNS) of flow and deformation performed using the commercial computational engineering platform by ANSYS. The simulations establish the range of validity of the theory, showing excellent agreement.

**Key words:** Keywords will be added during the typesetting process

---

## 1. Introduction

Microfluidics is the study of the manipulation of microscopic volumes of fluids at small scales (Squires & Quake 2005). Though the subfield of fluid mechanics pertaining to flows at small scales, i.e., *low Reynolds number hydrodynamics* (Happel & Brenner 1983), is not a new field, its relevance to technologies at the microscale (and thus the emergence of the term “microfluidics”) occurred only in the 1990s (Bruus 2008). Technological advancements in microfabrication over the past few decades (Xia & Whitesides 1998; Kitson *et al.* 2012; Su *et al.* 2016), also reviewed in by Nguyen & Wereley (2006), have made microscale fluid mechanics more accessible experimentally. The insights gained have been harnessed for a variety of applications, which in turn evinced keener interest in using microfluidics to solve global, medial and social problems (Whitesides 2006). The symbiotic relationship between basic science and human health is one of the most vivid manifestations of the potential of microfluidics research. For example,

† Email address for correspondence: christov@purdue.edu; url: <http://tmnt-lab.org>

technological applications of microfluidics include electronic chip cooling (Weisberg *et al.* 1992; Dixit & Ghosh 2015), lab-on-a-chip devices (Abgrall & Gué 2007) such as lab-on-a-CD diagnostics (Madou *et al.* 2006; Kong *et al.* 2016), *in vitro* isolation of cancer cells (Nagrath *et al.* 2007) and clinical pathology (Sun *et al.* 2010), and various micro-total analysis ( $\mu$ TAS) systems (Reyes *et al.* 2002; Auroux *et al.* 2002), among others. Microfluidic devices afford many advantages over their traditional counterparts: portability, low reagent consumption and short analyses times, often at higher resolutions than macroscopic counterparts (Nguyen & Wereley 2006).

A pernicious feature of microscale fluid mechanics is that fluid–structure interactions (FSIs) occur in both external and confined flows due to the compliance of the various solid-wall materials (Duprat & Stone 2016; Karan *et al.* 2018). For example, in inertialess locomotion (i.e., at low Reynolds number), a swimmer may be deformable (e.g., a bacterium has a flexible flagellum) or the fluid may be “deformable” (e.g., a polymeric substance dissolved into a liquid). On the one hand, in external flows, the elasticity of a swimmer affects its propulsive thrust and ability to navigate (Lauga 2016). On the other hand, in confined flows, the flow conduit may be made of a deformable material (Karan *et al.* 2018), such as polydimethylsiloxane (PDMS) (a polymeric gel) (Xia & Whitesides 1998) or elastin (a constituent of arteries) (Sandberg *et al.* 1977). Then, “creeping” flows can delaminate an elastic membrane from a solid boundary, forming blisters (Chopin *et al.* 2008), which are prone to a wealth of mechanical instabilities (Juel *et al.* 2018) and whose inflation dynamics are sensitive to the contact line conditions (Hewitt *et al.* 2015). The hydrodynamic pressure within such conduits is affected by their deformation due to two-way FSI. Specifically, the pressure drop across a soft microchannel is significantly smaller compared to the rigid case (Gervais *et al.* 2006). Consequently, deviations are expected from the classical *Hagen–Poiseuille law* (Sutera & Skalak 1993), which relates the viscous pressure drop across a length of pipe to the volumetric flow rate through it, the fluid properties and the physical dimensions. The goal of this study of *microscale fluid–structure interactions* is to mathematically analyze and quantify such deviations.

Extensive experimental work over the past decade has sought to understand FSI in microfluidics, specifically the effect of FSI on the flow rate–pressure drop relationship in a soft microchannel (Gervais *et al.* 2006; Hardy *et al.* 2009; Seker *et al.* 2009; Ozsun *et al.* 2013; Kang *et al.* 2014; Raj *et al.* 2017). In one of the earliest works, Gervais *et al.* (2006) employed a scaling analysis to determine a relation between the maximal channel deformation and the hydrodynamic pressure within a soft PDMS-based microchannel. The top wall of the microchannel was allowed to be compliant, while the remaining three walls were held rigid. By inserting said scaling relationship into the Hagen–Poiseuille law for a rectangular microchannel, Gervais *et al.* (2006) captured the observed nonlinear (quartic) relationship between the flow rate and the pressure drop for a Newtonian fluid (water). However, the approach of Gervais *et al.* (2006) is not predictive because it contains a fitting parameter (the unknown proportionality constant in the scaling relationship), which has to be determined *a posteriori* by experiments.

Christov *et al.* (2018) analyzed the problem of steady FSI in a microchannel via perturbation methods. Specifically, they determined the flow rate–pressure drop relation for a long, shallow microchannel with a compliant top wall by coupling a Kirchhoff–Love thin-plate theory to viscous flow under the lubrication approximation. Confirming the observation of Gervais *et al.* (2006), it was shown by Christov *et al.* (2018) that the flow rate–pressure drop relation is a quartic polynomial and the fitting parameter was thus eliminated through mathematical analysis. This approach was extended by Shidhore & Christov (2018) to capture thick top walls, via the first-order shear de-

formation plate theory of Mindlin (1951), and the predictions were extensively validated computationally via three-dimensional (3D) two-way coupled direct numerical simulations. More importantly, however, in (Christov *et al.* 2018; Shidhore & Christov 2018) the cross-sectional deformation profile of the microchannel’s compliant wall was determined. The perturbation approach’s generality is appealing as, in theory, higher-order corrections to the flow rate–pressure drop relation can be obtained along the lines of Tavakol *et al.* (2017), who developed an *extended* lubrication theory. Their approach is valid for channels with modest aspect ratios and with shape changes on the order of the channel height.

The study of moderate Reynolds number instabilities due to FSIs in soft tubes is a time-honored subject (Grotberg 1994; Grotberg & Jensen 2004; Heil & Hazel 2011) primarily due to their relevance in modeling biological flow in the arteries and the lungs. Consequently, microtubes traditionally reside on the opposite end of the FSI spectrum from microchannels, in terms of Reynolds number. Specifically, the study of *collapsible tubes* interrogates the case of microtubes whose radius *decreases* owing to a negative transmural pressure difference, eventually completely collapsing (Shapiro 1977; Bertram & Pedley 1982). Here, the flow field is approximated as one-dimensional, by averaging across the cross-section, but it is not fully-developed (Shapiro 1977). Viscous effects are captured using a pipe flow friction factor. A *tube law* is obtained to relate the local transmural pressure difference to the change in area due to circumferential and axial bending and tension, from postulated simple relations (Shapiro 1977) to rigorous derivations from shell theory (Whittaker *et al.* 2010). Even though the problem of collapsible tubes involves viscous flow, Shapiro (1977) elegantly explained the analogy to gas dynamics: a *speed index*, akin to the Mach number, divides the flow into subcritical and supercritical regimes. The relevance of this moderate-to-high Reynolds number FSI in soft tubes is evident in biofluid mechanics (Pedley 1980; Kizilova *et al.* 2012), for example in the contraction of the trachea during coughing (Grotberg 1994). The mathematical analysis of stability of such flows in 3D is an ongoing challenge (Gay-Balmaz *et al.* 2018). Nevertheless, there is also a need to develop accurate models for low Reynolds Number FSI in soft tubes due to the relevance to blood flow through small arteries (Čanić & Mikelić 2003).

Most the latter research has focused on Newtonian fluids. Biofluids are, however, non-Newtonian (Chakraborty 2005; Lee 2006). Blood is often modeled a Casson fluid, which has both a yield stress and a shear-dependent viscosity (Fung 1993, Ch. 3). Research on microscale FSIs has only just begun to take into account the non-Newtonian nature of the working fluids (Raj & Sen 2016; Boyko *et al.* 2017; Raj M *et al.* 2018; Anand *et al.* 2019). With further relevance to biofluid mechanics, Raj M *et al.* (2018) performed experiments on FSIs in a microchannel with *circular* cross-section, which is more akin to a microtube, or a blood vessel. The microchannel was fabricated from PDMS using a pull-out soft lithography process. A non-Newtonian blood-analog fluid (xanthan gum) was pumped through the microchannel. Measurements of the pressure drop at different inlet flow rates was shown to match a simple mathematical model of one-way FSI, meaning that the pressure was calculated using the Hagen–Poiseuille law for a rigid tube and then imposed as a load on the structure, without coupling the microchannel shape change back into the hydrodynamic pressure. Microtubes and microchannels of circular cross-section are now of significant scientific interest due to “a new, direct peeling-based technique for building long and thin, highly deformable microtubes” (Paek *et al.* 2015), which can be used in building bioinspired and biocompatible soft devices (Wu *et al.* 2018).

In a recent series of works (Elbaz & Gat 2014, 2016; Boyko *et al.* 2017), two-way coupling was captured through a mathematical analysis of the transient pressure and

deformation characteristics of a shallow, deformable microtube. Employing the Love–Kirchhoff hypothesis, a relation was obtained between the internal pressure load in a soft tube and its radial and axial deformations, up to the leading order in slenderness. Treating the structural problem as quasi-static, an unsteady diffusion-like equation for the fluid pressure was obtained and analyzed for both Newtonian (Elbaz & Gat 2014, 2016) and non-Newtonian (Boyko *et al.* 2017) fluids. However, the effect of non-trivial deformation on the resulting flow rate–pressure drop relation for the microtube (transient or steady-state) was not considered or benchmarked against simulations and/or experiments. Anand *et al.* (2019) achieved the latter for non-Newtonian microchannel FSI, leaving the microtube case an open problem that we pursue in the present work.

Thus, it should be clear that microscale FSIs are an important problem in mechanics. More importantly, however, recent results in the literature (e.g., Elbaz & Gat 2014; Boyko *et al.* 2017; Christov *et al.* 2018) suggest that asymptotic and perturbation methods can capture these fluid–structure interactions. To this end, in this paper, we present a comprehensive theoretical and computational study of steady non-Newtonian FSIs in deformable microtubes. To capture the non-Newtonian rheology of biofluids, we employ the “generalized Newtonian fluid” model with a power-law shear-dependent viscosity, which is suitable for steady flows. To capture the compliance of the (initially) cylindrical flow conduit, we employ classical (linear) shell theories. In §2, we describe the problem of interest, specifying the physical domain and the notation. Then, in §3, we solve for the flow field under the lubrication approximation. In §4, we employ thin-shell theory to solve for the deformation field. We bring all this together in §5, where the flow and the deformation fields are coupled, yielding a complete theory of FSI between a non-Newtonian fluid and a microtube. In §6, the predictions of the theory developed in this paper are benchmarked against full two-way coupled, 3D direct numerical simulations (DNS) of steady-state FSI carried out using commercial computational engineering tools. The benchmark against DNS allows us to both validate our mathematical results as well as to determine the theory’s range of applicability. Finally, §7 summarizes our results and presents an outlook for future work. To make the present work self-contained, appendices are provided discussing the DNS approach (Appendix A), further mathematical results on the interplay between FSI and non-Newtonian rheology (Appendix B) and the relation of our work to textbook models of flow in elastic blood vessels (Appendix C).

## 2. Preliminaries

We consider an initially cylindrical flow conduit geometry. As shown in Fig. 1, the geometry is *slender*, i.e., its stream-wise dimension is much larger than its cross-sectional dimension, and *shallow* (or, *thin*), i.e., its thickness is much smaller than its cross-sectional dimension. The cylindrical coordinate system has its origin at the center of the inlet of the tube but it is displaced in Fig. 1 for clarity. The wall of the microtube has a finite thickness, and it is soft; hence, it deforms due to the fluid flow within it. Specifically, the microtube has an undeformed radius  $a$ , a constant length  $\ell$ , and constant (within the classical shell theories to be discussed below) thickness  $t$ . The radial deformation of the microtube is denoted by  $u_r(z)$  so that the radius of the deformed tube is  $R(z) = a + u_r(z)$ . Axisymmetry ensures that the latter only depend on the flow-wise coordinate  $z$ . The microtube’s wall is composed of a linearly elastic material with constant modulus of elasticity (Young’s modulus)  $E$  and a constant Poisson ratio  $\nu$ .

Fully-developed steady flow of a non-Newtonian fluid enters the microtube across the inlet ( $z = 0$  plane) at a constant flow rate  $q$ . The non-Newtonian behavior of the fluid is due to its shear-dependent viscosity. Our main objective is to determine the relation

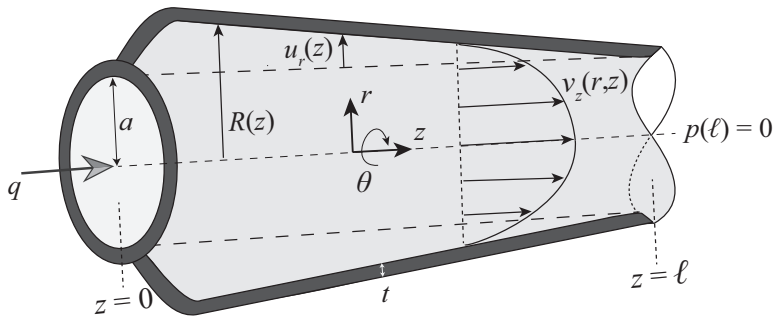


FIGURE 1. Schematic of the slender and thin microtube geometry in its deformed configuration. The notation for the flow and the deformation is also labeled. [Reprinted/adapted with permission from “On the Deformation of a Hyperelastic Tube Due to Steady Viscous Flow Within,” Vishal Anand, Ivan C. Christov, *Dynamical Processes in Generalized Continua and Structures*, *Advanced Structured Materials* **103**, pp. 17–35, doi:10.1007/978-3-030-11665-1\_2. © Springer Nature 2019].

between the pressure drop  $\Delta p$ , across the length of the microtube, and the imposed flow rate  $q$ . In other words, we seek to derive, mathematically, the Hagen–Poiseuille law for steady non-Newtonian flow in a deformable tube. To this end, we simplify the fluid flow (§3) and structural mechanics (§4) problems independently in the appropriate asymptotic limit(s). Then, we solve the two sets of governing equations, which are coupled together by the hydrodynamic pressure (the normal forces exerted by the fluid), which act as a load on the structure.

### 3. Fluid mechanics problem

The assumptions made pertaining to the fluid flow problem are:

- (i) Steady flow:  $\partial(\cdot)/\partial t = 0$ .
- (ii) Axisymmetric flow:  $\partial(\cdot)/\partial\theta = 0$  and  $v_\theta = 0$ .
- (iii) Slender tube:  $\ell \gg a \Leftrightarrow \epsilon := a/\ell \ll 1$ .

Assumption (iii) is key to our analysis. Davis (2017) highlights the “importance of being thin” in making analytical progress on nonlinear fluid mechanics problems.

First, we determine the kinematics of the flow. In the cylindrical coordinates labeled in Fig. 1, and under assumption (ii) above, the fluid’s equation of continuity (conservation of mass) is

$$\frac{1}{r} \frac{\partial}{\partial r}(r v_r) + \frac{\partial v_z}{\partial z} = 0. \quad (3.1)$$

Let us now introduce the following dimensionless variables:

$$\bar{r} = r/a, \quad \bar{p} = p/\mathcal{P}_c, \quad \bar{z} = z/\ell, \quad \bar{v}_z = v_z/\mathcal{V}_z, \quad \bar{v}_r = v_r/\mathcal{V}_r, \quad (3.2a, b, c, d, e)$$

Here,  $\mathcal{V}_z$  and  $\mathcal{V}_r$  are characteristic velocity scales in the axial and radial directions respectively, while  $\mathcal{P}_c$  is the characteristic pressure scale: e.g., the full pressure drop in pressure-controlled scenarios or the viscous pressure scale in flow-rate-controlled situations.  $\mathcal{P}_c$  can be determined from the velocity scale [see Eq. (3.10) below]. Introducing the dimensionless variables from Eq. (3.2), Eq. (3.1) becomes

$$\frac{1}{\bar{r}} \frac{\partial}{\partial \bar{r}}(\bar{r} \bar{v}_r) \frac{\mathcal{V}_r}{a} + \frac{\partial \bar{v}_z}{\partial \bar{z}} \frac{\mathcal{V}_z}{\ell} = 0. \quad (3.3)$$

Balancing all terms in Eq. (3.3) yields the characteristic radial velocity scale:  $\mathcal{V}_r \equiv \epsilon \mathcal{V}_z$ .

Consequently, to the leading order in  $\epsilon$ , the velocity field is *unidirectional* (Leal 2007):  $\bar{\mathbf{v}} = \bar{v}_z(\bar{r})\hat{\mathbf{k}}$ , where  $\hat{\mathbf{k}}$  is the unit normal vector in the  $z$ -direction. Below, we show that, due to FSI, the unidirectional profile “picks up” a weak  $\bar{z}$  dependence as well, which is “allowed” under the *lubrication approximation* (Leal 2007; Bruus 2008).

Next, we consider the dynamics of the flow field. Since we are dealing with flow at the microscale, the Reynolds number  $Re$  (to be properly defined below upon introducing the fluid’s rheology) is assumed to be small (i.e.,  $Re \ll 1$ ), and the lubrication approximation applies. Consequently, inertial forces in fluid are negligible in comparison to pressure and viscous forces, and we begin our analysis with the following simplified equations expressing the momentum conservation in the (radial)  $r$ - and (axial)  $z$ -directions (Bird *et al.* 1987):

$$0 = \frac{1}{r} \frac{\partial}{\partial r} (r\tau_{rr}) + \frac{\partial \tau_{zr}}{\partial z} - \frac{\tau_{\theta\theta}}{r} - \frac{\partial p}{\partial r}, \quad (3.4a)$$

$$0 = \frac{1}{r} \frac{\partial}{\partial r} (r\tau_{rz}) + \frac{\partial \tau_{zz}}{\partial z} - \frac{\partial p}{\partial z}. \quad (3.4b)$$

Here,  $\boldsymbol{\tau}$  is the fluid’s shear stress tensor, and  $p$  is the hydrodynamic pressure. We have already made use of the assumptions of axisymmetry in Eqs. (3.4). The same assumption also leads to the momentum equation in  $\theta$  direction being reduced to zero *identically*.

Now, we need to express the rate-of-strain tensor  $\dot{\boldsymbol{\gamma}}$  in terms of the velocity components. It is wise to use all the results (axisymmetric unidirectional flow with only a  $z$ -component) so far to simplify this calculation. Then, for the chosen cylindrical coordinate system, the only non-vanishing rate-of-strain components (in terms of the velocity gradient) are

$$\dot{\gamma}_{zz} = 2 \frac{\partial v_z}{\partial z} = \frac{2\epsilon \mathcal{V}_z}{a} \frac{\partial \bar{v}_z}{\partial \bar{z}}, \quad (3.5a)$$

$$\dot{\gamma}_{rz} = \dot{\gamma}_{zr} = \frac{\partial v_r}{\partial z} + \frac{\partial v_z}{\partial r} = \frac{\partial v_z}{\partial r} = \frac{\mathcal{V}_z}{a} \frac{\partial \bar{v}_z}{\partial \bar{r}}, \quad (3.5b)$$

having used the dimensionless variables from Eq. (3.2). Clearly,  $(a/\mathcal{V}_z)\dot{\gamma}_{zz} = \mathcal{O}(\epsilon)$ , while  $(a/\mathcal{V}_z)\dot{\gamma}_{rz}$ ,  $(a/\mathcal{V}_z)\dot{\gamma}_{zr} = \mathcal{O}(1)$ . Therefore, to a leading order in  $\epsilon$ , the rate-of-strain tensor has two components, consistent with the kinematic reduction to unidirectional flow. Consequently, the only non-zero components of the shear stress tensor are  $\tau_{rz}$  and  $\tau_{zr}$ .

The argument based on Eqs. (3.5) can be generalized to show that  $\partial \tau_{zr}/\partial z$  is  $\mathcal{O}(\epsilon)$  compared to  $\partial p/\partial r$ . Taking all of these deliberations into account, the momentum conservation equations (3.4) reduce

$$0 = \frac{\partial p}{\partial r}, \quad (3.6a)$$

$$0 = \frac{1}{r} \frac{\partial}{\partial r} (r\tau_{rz}) - \frac{\partial p}{\partial z}. \quad (3.6b)$$

Equation (3.6a) implies that the pressure is at most a function of  $z$ , i.e.,  $p = p(z)$ . This result is as far as we can go at this stage. Next, we need to specify the constitutive equation relating  $\boldsymbol{\tau}$  to  $\dot{\boldsymbol{\gamma}}$  to connect the *kinematics* of the flow problem to its *dynamics*.

Keeping biofluid mechanics applications in mind, we consider the fluid to be non-Newtonian fluid. Blood is known to exhibit shear-dependent viscosity at steady state, and it is often modeled as a *Casson fluid*, which captures both a yields stress and a shear-dependent viscosity (Fung 1993, Ch. 3). However, detecting the yield stress (at zero shear rate) in a suspension of blood cells is extremely difficult (perhaps even “controversial” as discussed by Balmforth *et al.* (2014)), and some experiments (Chien *et al.* 1966) show it to be vanishing (see also Fung 1993, p. 65). Therefore, we consider the special case

of zero yield stress, which reduces the Casson fluid model to the *power-law fluid* (also known as Ostwald–de Waele (Bird 1976)) model. Then, utilizing Eq. (3.5b), the shear stress is expressed in terms of rate of strain as

$$\tau_{rz} = \eta \dot{\gamma}_{rz} = \eta \frac{\partial v_z}{\partial r}, \quad \eta = m \left| \frac{\partial v_z}{\partial r} \right|^{n-1}, \quad (3.7a, b)$$

where  $\eta$  is the *apparent viscosity*,  $m$  is the *consistency factor* (a non-negative real number), and  $n$  is the *power-law index* (also a non-negative real number). Now, the appropriate definition of the Reynolds number given the above non-dimensionalization and power-law rheology is  $Re = \rho a^n \mathcal{V}_z^{2-n} / m$  (see also Crespí-Llorens *et al.* 2015), where  $\rho$  is the fluid's density. As usual,  $n < 1$  corresponds to shear-thinning fluids, such as blood (Chien *et al.* 1966), in which the apparent viscosity decreases with shear rate. On the other hand,  $n > 1$  corresponds to shear-thickening fluids in which the apparent viscosity increases with shear rate, giving rise to applications for ballistic armor, such as woven Kevlar fabrics impregnated with a colloidal suspension of silica particles (Wagner & Brady 2009). Although the most common biofluid, namely blood, is shear-thinning or pseudoplastic ( $n < 1$ ), our analysis nevertheless captures Newtonian ( $n = 1$ , in which case  $m = \mu$  is the shear viscosity) and shear-thickening or dilatant ( $n > 1$ ) behavior as well, through the rheological model in Eq. (3.7).

For axisymmetric flow, we expect that the axial velocity will attain its maximum along the centerline ( $r = 0$ ), decreasing with the radius until it reaches zero at the tube wall (due to no slip) in this steady flow. Consequently, the velocity gradient is negative and  $|\partial v_z / \partial r| = -\partial v_z / \partial r$ . Then, in terms of the dimensionless variables, Eq. (3.7) becomes

$$\tau_{rz} = -m \left( \frac{\mathcal{V}_z}{a} \right)^n \left( -\frac{\partial \bar{v}_z}{\partial \bar{r}} \right)^n. \quad (3.8)$$

Substituting the latter expression for  $\tau_{rz}$  along with the dimensionless pressure into the  $z$ -momentum equation (3.6b) yields

$$\frac{1}{\bar{r}} \frac{\partial}{\partial \bar{r}} \left[ \bar{r} \left( -\frac{\partial \bar{v}_z}{\partial \bar{r}} \right)^n \right] = - \left( \frac{\mathcal{P}_c a^{n+1}}{\ell \mathcal{V}_z^n m} \right) \frac{d\bar{p}}{d\bar{z}}. \quad (3.9)$$

Since the terms on the left- and right-hand side of Eq. (3.9) must be both  $\mathcal{O}(1)$ , we deduce that the term in parentheses on the right hand side of the equation should be

$$\left( \frac{\mathcal{P}_c a^{n+1}}{\ell \mathcal{V}_z^n m} \right) \equiv 1 \quad \Leftrightarrow \quad \mathcal{V}_z = \left( \frac{a^{n+1} \mathcal{P}_c}{mL} \right)^{1/n}. \quad (3.10a, b)$$

This equation relates the velocity and pressure scales. In a flow-rate-controlled experiment/simulation, we can choose a velocity scale  $\mathcal{V}_z = q / (\pi a^2)$  based on the inlet flow rate  $q$ , and then the pressure scale  $\mathcal{P}_c$  can be calculated from Eq. (3.10). Thus, Eq. (3.9) becomes

$$\frac{\partial}{\partial \bar{r}} \left[ \bar{r} \left( -\frac{\partial \bar{v}_z}{\partial \bar{r}} \right)^n \right] = -\frac{d\bar{p}}{d\bar{z}} \bar{r}. \quad (3.11)$$

Integrating this equation with respect to  $\bar{r}$  and requiring that  $\bar{v}_z$  to be finite along the centerline as well as enforcing no slip,  $\bar{v}_z(\bar{r} = \bar{R}) = 0$ , yields

$$\bar{v}_z = \left( -\frac{1}{2} \frac{d\bar{p}}{d\bar{z}} \right)^{1/n} \left( \frac{\bar{R}^{1+1/n} - \bar{r}^{1+1/n}}{1 + 1/n} \right), \quad (3.12)$$

where  $\bar{R} = R/a$  is the dimensionless deformed microtube radius. Note that  $\bar{R}$  is not necessarily unity because we allow the microtube to deform due to FSI, as discussed in

the next section. As a result, while  $\bar{p}$  is at most a function of  $\bar{z}$ ,  $\bar{v}_z$  can depend upon both  $\bar{r}$  and  $\bar{z}$ .

#### 4. Structural mechanics problem

In §3, the 3D momentum conservation equations for a power-law fluid were reduced to unidirectional flow. They explicitly dependent only on the radial coordinate, up to the leading order. This simplification was achieved by prudently harnessing the assumptions of axisymmetry and slenderness, along with the lubrication approximation.

In a similar manner, we now proceed to tackle the structural mechanics problem of the tube's deformation. The equations stating the equilibrium of forces in this problem are again three dimensional. To reduce the dimensionality of the problem, and make it tractable analytically, we employ some simplifying assumptions:

- (i) The cylinder is thin; its thickness is negligible compared to its radius:  $t \ll a$ .
- (ii) The cylinder is slender; its radius is small compared to its length:  $a \ll \ell$ .
- (iii) The material from which the tube is composed is isotropic and linearly elastic, with elasticity (Young's) modulus  $E$  and Poisson ratio  $\nu$ , so the relationship between stress and strain is linear. Furthermore, the material is assumed to be a soft rubber-like elastomer (i.e., "small"  $E$  and  $\nu \approx 1/2$ ).
- (iv) The strains are small, so the relationship between strain and displacement is linear.
- (v) The characteristic radial deformation  $\mathcal{U}_c$  is small compared to the (smallest) characteristic dimension of the cylinder:  $\mathcal{U}_c \ll t$ .

Here, assumptions (iii) and (iv) ensure that the relation between stress and displacement is linear. Thus, the corresponding theory developed in this paper pertains to what we shall term *linear* FSI. The ramifications of assumptions (i) and (ii) will be discussed in the context of shell theories. Assumption (v) implies our theory is a *small-deformation* FSI theory, thus we may work the problem in Eulerian coordinates.

A *shell* is materialization of a surface and, hence, is a 3D entity by definition (Flügge 1960). A *shell theory* attempts to capture the dynamics of a shell in two dimensions and is *de jure* an approximate theory. Approximations are introduced in every facet of shell theory, namely the strain–displacement relation (*kinematics*), the stress equilibrium relation (*statics*), and the stress–strain relation (*constitutive*). There are many shell theories, of varying degree of approximation, and the treatment here cannot be exhaustive. For further details, the reader is directed to the classic monographs by Kraus (1967), Flügge (1960), and Timoshenko & Woinowsky-Krieger (1959). We focus only on the "simplest" shell theories capable of describing the FSI problem posed above.

##### 4.1. Membrane theory

Owing to the thinness assumption ( $t \ll a$ ), the microtube can be analyzed using membrane theory for sufficiently small  $t/a$ . Membrane theory of shells pertains to structures that sustain only tension (in the axial and/or in the circumferential directions) but cannot support bending or twisting moments (Flügge 1960, Ch. 3).<sup>†</sup>

There are, apparently, two approaches to the problem of stress distribution in and deformation of a cylindrical membrane clamped at both ends. The first approach (see, e.g., Olufsen *et al.* 2000) is to make the assumption that the axial displacement  $u_z \equiv 0$

<sup>†</sup> This membrane theory is to be contrasted to, e.g., the highly nonlinear Föppl–von Kármán theory (Timoshenko & Woinowsky-Krieger 1959) of topologically rectangular thin plates (also often termed membranes).



*a priori*. From the constitutive equation of linear elasticity, we then have

$$u_z = \varepsilon_{zz}\ell = (\sigma_{zz} - \nu\sigma_{\theta\theta})\frac{\ell}{E}, \quad (4.1)$$

where  $\sigma_{\theta\theta}$  is the hoop stress, while  $\sigma_{zz}$  and  $\varepsilon_{zz}$  are the axial stress and strain, respectively. Together with the assumption of  $u_z \equiv 0$ , Eq. (4.1) yields

$$\sigma_{zz} = \nu\sigma_{\theta\theta}. \quad (4.2)$$

To find an expression for  $\sigma_{\theta\theta}$ , we appeal to the equation of static equilibrium in the circumferential direction:

$$N_\theta = ap, \quad (4.3)$$

where  $N_\theta$  is the stress resultant in the azimuthal direction of the tube. Here, the hydrodynamic pressure  $p(z)$  provides the load, and we have shown in §3 that  $p$  is, at most, a function of  $z$ . Next, membrane theory assumes that due to the cylinder being thin, the stress across the thickness is uniform. Therefore,  $\sigma_{\theta\theta}$  is simply the corresponding stress resultant divided by the cylinder's thickness  $t$ :

$$\sigma_{\theta\theta} = \frac{N_\theta}{t} = \left(\frac{a}{t}\right)p. \quad (4.4)$$

Finally, from the equivalent of Eq. (4.1) for the radial displacement and Eqs. (4.2) and (4.4), we obtain

$$u_r(z) = \varepsilon_{\theta\theta}a = (\sigma_{\theta\theta} - \nu\sigma_{zz})\frac{a}{E} = (1 - \nu^2)\left(\frac{a^2}{Et}\right)p(z). \quad (4.5)$$

The second approach in the literature (see, e.g., Čanić & Mikelić 2003) is to start with the force equilibrium in the axial direction:

$$\frac{dN_z}{dz} + \mathcal{T}_z = 0, \quad (4.6)$$

where  $N_z$  is the stress resultant in the  $z$ -direction and  $\mathcal{T}_z$  is the shear stress acting on the wall of the tube. The shear stress acting on the tube must be equal and opposite to the shear stress in the fluid at the wall:

$$\mathcal{T}_z = -\tau_{rz}|_{r=a} = -\frac{a}{2}\frac{\partial p}{\partial z}, \quad (4.7)$$

having used Eq. (3.6*b*). In light of the perturbative approach established for microchannels (Christov *et al.* 2018), in which the shear stresses on the structure are asymptotically smaller than the normal stresses, Eq. (4.7) is a puzzling starting point. Using Eq. (4.7), Eq. (4.6) can be integrated to yield

$$N_z = \left(\frac{a}{2}\right)p + C, \quad (4.8)$$

where  $C = N_z(z = \ell)$  [since  $p(z = \ell) = 0$  is our pressure outlet boundary condition] is unknown. As before, the membrane theory assumes that the stresses are uniform across the thickness, therefore the axial stress is simply

$$\sigma_{zz} = \frac{N_z}{t} = \left(\frac{a}{2t}\right)p + \frac{C}{t}, \quad (4.9)$$

whilst the expression for hoop stress is still Eq. (4.4). As in Eq. (4.5), we obtain the

radial displacement

$$u_r(z) = \left(1 - \frac{\nu}{2}\right) \left(\frac{a^2}{Et}\right) p(z) - \frac{\nu a C}{Et}. \quad (4.10)$$

For the  $z = \ell$  end of the cylinder to be clamped,  $u_r(z = \ell) = 0$ , we must take  $C = 0$  because  $p(z = \ell) = 0$ . Then, the radial displacement becomes

$$u_r(z) = \left(1 - \frac{\nu}{2}\right) \left(\frac{a^2}{Et}\right) p(z). \quad (4.11)$$

Notice the factor involving the Poisson ratio is different in Eq. (4.5) than in Eq. (4.11). Similarly, the axial displacement is found using Eq. (4.1):

$$u_z(z) = \varepsilon_{zz}\ell = (\sigma_{zz} - \nu\sigma_{\theta\theta})\frac{\ell}{E} = \left(\frac{1}{2} - \nu\right) \left(\frac{a\ell}{Et}\right) p(z). \quad (4.12)$$

Therefore, in this second formulation of the problem,  $u_z = 0$  identically *only* for an incompressible material ( $\nu = 1/2$ ).

In summary, the expression for the radial deformation,  $u_r(z)$  is given by

$$u_r(z) = \left(\frac{a^2}{Et}\right) p(z) \times \begin{cases} (1 - \nu^2), & \text{if } u_z \equiv 0, \\ (1 - \nu/2), & \text{if } C = 0. \end{cases} \quad (4.13)$$

Without much of an explanation, both the latter expressions for  $u_r(z)$  have been presented in literature almost interchangeably (Olufsen *et al.* 2000; Čanić & Mikelić 2003). Clearly, the two expressions differ by a factor  $\propto (1/2 - \nu)\nu$  (a small quantity for nearly incompressible rubber-like elastomers); for incompressible materials ( $\nu = 1/2$ ), the two expressions agree identically. Indeed, as the above deliberations show, the assumptions of  $C = 0$ ,  $u_z \equiv 0$  and  $\nu = 1/2$  are interlinked. However, it is also true that  $C = 0$  holds, in some cases, even if the material is *not* incompressible; for example when the outlet end of the microtube is free [thus, *both*  $N_z(z = \ell) = 0$  and  $p(z = \ell) = 0$ ] as in the problem discussed by Elbaz & Gat (2014). Thus, while the above approaches to the deformation of a cylinder clamped at both ends are inconsistent (do not yield an equivalent expression for the radial displacement), the quantitative difference is small because  $(1 - \nu^2) \approx (1 - \nu/2) \approx 3/4$  for an almost-incompressible material ( $\nu \approx 1/2$ ), and we proceed under the assumption that  $u_z = 0$ .

Finally, the most important conclusion to be drawn from the analysis in this subsection is that, under the membrane theory, the microtube's radial displacement is simply proportional to the local hydrodynamic pressure, with the geometric and elasticity parameters setting the proportionality constant.

#### 4.2. Donnell shell theory

From the several theories for thin shells of revolution based on the Love–Kirchhoff hypothesis (Love 1888), perhaps the earliest and most “popular” is Donnell’s shell theory (Donnell 1933). Donnell’s shell theory is a straightforward extension of thin-plate theory to shells (Kraus 1967), which itself is an extension of Euler-beam theory to two dimensions. Furthermore, for the special case of axisymmetric loads with zero curvature, Donnell’s shell theory reduces identically to the Love–Kirchhoff thin-plate theory (Kraus 1967), which we have successfully employed to analyze microchannel FSIs (Christov *et al.* 2018; Anand *et al.* 2019). Improving upon the membrane theory of §4.1, Donnell’s shell theory takes into account bending and, in the case of non-axisymmetry, twisting moments of the microtube (Kraus 1967).

To be consistent with the membrane theory of §4.1, we again neglect the axial displacement (i.e., we take  $u_z \equiv 0$ ). In fact, it has also been shown by Čanić *et al.* (2007), starting from large-deformation elasticity theory of an incompressible tube tethered longitudinally at both ends, that  $u_z \approx 0$  in the limit of a slender tube (i.e.,  $a/\ell \rightarrow 0^+$ ). Then, following Dym (1990, Ch. V), the equation expressing the momentum balance (for axisymmetric deformation and loading) of Donnell's shell theory is

$$\frac{d^2 M_z}{dz^2} - \frac{N_\theta}{a} = -p(z). \quad (4.14)$$

Here, the bending moment  $M_z$  is expressed through the elastic law as

$$M_z = -K \frac{d^2 u_r}{dz^2}, \quad (4.15)$$

where  $K = Et^3/[12(1 - \nu^2)]$  is the *bending (flexural) rigidity* of the shell. The stress resultant in the circumferential direction is

$$N_\theta = D \left( \frac{u_r}{a} \right), \quad (4.16)$$

where  $D = Et/(1 - \nu^2)$  is the *extensional rigidity* of the shell. Then, Eq. (4.14), when written in terms of the displacement using Eqs. (4.15) and (4.16), and simplified by substituting the expressions for  $D$  and  $K$ , becomes an ordinary differential equation (ODE) for the radial deflection  $u_r(z)$  forced by the hydrodynamic pressure  $p(z)$ :

$$\frac{Et^3}{12(1 - \nu^2)} \left( \frac{d^4 u_r}{dz^4} + \frac{12}{a^2 t^2} u_r \right) = p. \quad (4.17)$$

To understand the dominant balance(s) in Eq. (4.17), we introduce dimensionless variables, some of which are restated from Eq. (3.2), as follows:

$$\bar{z} = z/\ell, \quad \bar{u}_{\bar{r}} = u_r/\mathcal{U}_c, \quad \bar{p} = p/\mathcal{P}_c, \quad (4.18a, b, c)$$

where, as before,  $\mathcal{P}_c$  is the characteristic pressure scale. The characteristic scale for the radial deflection of the tube,  $\mathcal{U}_c$ , is to be determined self-consistently as part of this analysis. Substituting the dimensionless variables from Eq. (4.18) into Eq. (4.17) yields

$$\left( \frac{t}{a} \right)^2 \left( \frac{a}{\ell} \right)^4 \frac{d^4 \bar{u}_{\bar{r}}}{d\bar{z}^4} + 12 \bar{u}_{\bar{r}} = \frac{12(1 - \nu^2)a^2 \mathcal{P}_c}{Et \mathcal{U}_c} \bar{p}. \quad (4.19)$$

For a thin and slender shell we can neglect, in an order of magnitude sense to the leading order in  $t/a$  and  $a/\ell$ , the first term on the left-hand side of Eq. (4.19) to obtain:

$$\bar{u}_{\bar{r}} = \frac{a^2 \mathcal{P}_c}{Et \mathcal{U}_c} (1 - \nu^2) \bar{p}. \quad (4.20)$$

Since Eq. (4.20) represents a leading-order balance, comparing coefficients on both sides of the equation yields the deformation scale

$$\mathcal{U}_c = \frac{a^2 \mathcal{P}_c}{Et}. \quad (4.21)$$

Hence, the deformed tube radius is

$$\bar{R}(\bar{z}) \equiv \frac{a + u_r(z)}{a} = 1 + \beta \bar{u}_{\bar{r}}(\bar{z}), \quad (4.22)$$

where  $\beta := \mathcal{U}_c/a$  is a dimensionless parameter that controls the fluid–structure interaction. It is a measure of the magnitude of the characteristic wall deformation  $\mathcal{U}_c$  compared

to the undeformed radius  $a$ . A larger value of  $\beta$  corresponds to “stronger” fluid–structure coupling and, thus, a larger deformation.

Thus, at the leading order in  $t/a$  and  $a/\ell$ , Eq. (4.19) yields a simple deformation–pressure relation:

$$\bar{u}_{\bar{r}}(\bar{z}) = (1 - \nu^2)\bar{p}(\bar{z}). \quad (4.23)$$

Note that Eq. (4.23) is identically the dimensionless version of our membrane theory result in Eq. (4.5).

REMARK 1. *To the leading order in  $t/a$  and  $a/\ell$ , the shell theory considered here yields the same equation as membrane theory, namely Eq. (4.5), which dictates that the radial deflection of the tube is directly proportional to the pressure at a given flow-wise cross-section. This observation is in agreement with the results of Elbaz & Gat (2014, 2016), taking into account, of course, the different boundary conditions employed therein.*

REMARK 2. *Equation (4.23) can also be derived by letting the bending rigidity  $K \rightarrow 0^+$  in Donnell’s shell theory. This observation shows that, in the limit of negligible bending, the shell theory self-consistently reduces to the membrane theory.*

## 5. Coupling the fluid mechanics and structural problems: Flow rate–pressure drop relation

We now turn to the main task, which is evaluating the pressure drop as function of the flow rate and thus generalizing the Hagen–Poiseuille law to deformable microtubes. The flow rate in the microtube is by definition

$$q = \int_0^{2\pi} \int_0^{R(z)} v_z r \, dr \, d\theta = \mathcal{V}_z 2\pi a^2 \int_0^{\bar{R}(\bar{z})} \bar{v}_{\bar{z}} \bar{r} \, d\bar{r}, \quad (5.1)$$

where the second equality follows from performing the (trivial) azimuthal integration, introducing the dimensionless variables from Eq. (3.2), and changing the integration limits. Note that, in general,  $\bar{v}_{\bar{z}} = \bar{v}_{\bar{z}}(\bar{r}, \bar{z} + \bar{u}_{\bar{z}})$  in the last expression. However, since we have assumed  $\bar{u}_{\bar{z}} = 0$ , then we can evaluate it as  $\bar{v}_{\bar{z}}(\bar{r}, \bar{z})$ . Now, substituting the expression for  $\bar{v}_{\bar{z}}$  from Eq. (3.12) into Eq. (5.1):

$$\begin{aligned} q &= \mathcal{V}_z 2\pi a^2 \int_0^{\bar{R}(\bar{z})} \left( -\frac{1}{2} \frac{d\bar{p}}{d\bar{z}} \right)^{1/n} \frac{[\bar{R}(\bar{z})]^{1+1/n} - \bar{r}^{1+1/n}}{1 + 1/n} \bar{r} \, d\bar{r} \\ &= \mathcal{V}_z \pi a^2 \left( -\frac{1}{2} \frac{d\bar{p}}{d\bar{z}} \right)^{1/n} \frac{[\bar{R}(\bar{z})]^{3+1/n}}{3 + 1/n}. \end{aligned} \quad (5.2)$$

Henceforth, we use the dimensionless flow rate  $\bar{q} = q/(\mathcal{V}_z \pi a^2)$ . In a steady flow, conservation of mass requires that  $q$  is a constant independent of  $z$ , thus Eq. (5.2) is an ODE for  $\bar{p}(\bar{z})$ , subject to an appropriate closure relation for  $\bar{R}(\bar{z})$ .

### 5.1. Rigid tube

First, for completeness and future reference, consider the case of  $\bar{R} = 1$  (rigid tube of uniform radius). Equation (5.2) can be immediately integrated to yield the usual linear pressure profile:

$$\bar{p}(\bar{z}) = 2[(3 + 1/n)\bar{q}]^n (1 - \bar{z}). \quad (5.3)$$

Since it is our convention that  $\bar{p}(\bar{z} = 0) = \Delta\bar{p}$  is the full pressure drop across the microtube, then

$$\Delta\bar{p} = 2[(3 + 1/n)\bar{q}]^n, \quad (5.4)$$

which is the well-known Hagen–Poiseuille law for a power-law fluid (Bird *et al.* 1987).

### 5.2. Leading-order-in-thickness (membrane) theory

Next, inserting the relation  $\bar{R} = 1 + (1 - \nu^2)\beta\bar{p}$  [having employed Eqs. (4.22) and (4.23)] into Eq. (5.2) yields an ODE for  $\bar{p}(\bar{z})$  given  $\bar{q}$ :

$$\frac{d\bar{p}}{d\bar{z}} = -2[(3 + 1/n)\bar{q}]^n [1 + (1 - \nu^2)\beta\bar{p}]^{-(3n+1)}. \quad (5.5)$$

Separating variables and integrating, subject to the outlet boundary condition  $[\bar{p}(1) = 0]$  we have:

$$\bar{q}^n(\bar{z} - 1) = \frac{1 - [1 + (1 - \nu^2)\beta\bar{p}]^{3n+2}}{2(3 + 1/n)^n(3n + 2)(1 - \nu^2)\beta}. \quad (5.6)$$

Equation (5.6) is an *implicit* relation for  $\bar{p}$  (given  $\bar{q}$ ), which [unlike the case of microchannels (Christov *et al.* 2018; Shidhore & Christov 2018; Anand *et al.* 2019)] can be inverted to yield

$$\bar{p}(\bar{z}) = \frac{1}{(1 - \nu^2)\beta} \left\{ [1 - 2(3n + 2)(1 - \nu^2)\beta[(3 + 1/n)\bar{q}]^n(\bar{z} - 1)]^{1/(3n+2)} - 1 \right\}. \quad (5.7)$$

The flow rate–pressure drop relation is obtained by evaluating Eq. (5.6) at  $\bar{z} = 0$ :

$$\bar{q} = \left( \frac{1}{2(3 + 1/n)^n(3n + 2)(1 - \nu^2)\beta} \left\{ [1 + (1 - \nu^2)\beta\Delta\bar{p}]^{(3n+2)} - 1 \right\} \right)^{1/n}. \quad (5.8)$$

REMARK 3. Equation (5.5) can be inverted to yield the flow rate in terms of the pressure gradient:

$$\bar{q} = \sigma(\bar{p}) \left( -\frac{d\bar{p}}{d\bar{z}} \right)^{1/n}, \quad \sigma(\bar{p}) := \frac{1}{3 + 1/n} \left\{ \frac{1}{2} [1 + (1 - \nu^2)\beta\bar{p}]^{(3n+1)} \right\}^{1/n}. \quad (5.9a, b)$$

The form of this equation is, clearly, a generalization of the classic result of Rubinow & Keller (1972) for steady low  $Re$ , Newtonian flow in a deformable tube. More importantly, however, we have also self-consistently derived the function  $\sigma$  that accounts for steady non-Newtonian FSI in a microtube.

REMARK 4. The maximum displacement of the microtube wall over its length [recall Eq. (4.22)] is given by  $\beta\bar{u}_{\bar{r}}(\bar{0})$ , which can be re-expressed, via Eq. (4.23), as  $(1 - \nu^2)\beta\bar{p}(0)$ . Now,  $\bar{p}(0)$  can be inserted from Eq. (5.7) to ultimately yield, under the leading-order-in-thickness theory,

$$\max_{0 \leq \bar{z} \leq 1} \beta\bar{u}_{\bar{r}}(\bar{z}) = \left\{ 1 + 2(3n + 2)(1 - \nu^2)\beta[(3 + 1/n)\bar{q}]^n \right\}^{1/(3n+2)} - 1. \quad (5.10)$$

Note that, once the solid and fluid properties ( $\nu$  and  $n$ ) are fixed, the maximum displacement is solely a function of the dimensionless flow rate  $\bar{q}$  and the FSI parameter  $\beta$ . The maximum displacement is thus larger for shear-thinning fluids compared to shear-thickening fluids, except at low values of  $\beta$ . This complex interplay of  $\beta$  and  $n$  is discussed more thoroughly in §6 and in Appendix B.

REMARK 5. To perform the consistency check of recovering the rigid-tube pressure profile in Eq. (5.3) as the  $\beta \rightarrow 0^+$  limit of the deformable-tube pressure profile in Eq. (5.7), we must realize that  $\beta \rightarrow 0^+$  in Eq. (5.7) is a “0/0” limit. L’Hôpital’s rule or a Taylor series in  $\beta \ll 1$  easily shows that Eq. (5.3) is indeed the  $\beta \rightarrow 0^+$  limit of Eq. (5.7).

### 5.2.1. Special case of FSI in a microtube due to flow of a Newtonian fluid

Now, let us consider the case of a Newtonian fluid (i.e.,  $n = 1$  and  $m = \mu$ ) of Eq. (5.7):

$$\bar{p}(\bar{z}) = \frac{1}{(1 - \nu^2)\beta} \left\{ [1 - 40(1 - \nu^2)\beta\bar{q}(\bar{z} - 1)]^{1/5} - 1 \right\}. \quad (5.11)$$

Meanwhile, from Eq. (5.8), we have

$$\bar{q} = \frac{1}{40(1 - \nu^2)\beta} \left\{ [1 + (1 - \nu^2)\beta\Delta\bar{p}]^5 - 1 \right\}. \quad (5.12)$$

### 5.3. Beyond leading-order-in-thickness theory

In §5.2, we obtained the flow rate–pressure drop relationship considering only the leading-order deformation profile as given by Eq. (4.23). In this subsection, we venture beyond the leading-order approximation by solving the “full” ODE (4.17) for the deformation under Donnell’s shell theory. Equation (4.17) is coupled to Eq. (5.2), which relates the flow rate to the pressure gradient and the microtube’s radial deformation.

For clarity, we start from the dimensional equations and non-dimensionalize. Equation (5.2), in dimensional variables, takes the form

$$\frac{dp}{dz} = \left[ \frac{(3 + 1/n)q}{\pi} \right]^n \left[ \frac{-2m}{(a + u_r)^{3n+1}} \right]. \quad (5.13)$$

Next, taking  $d/dz$  of Eq. (4.17) and substituting Eq. (5.13) into the latter yields a single *nonlinear* fifth-order ODE in the deformation:

$$\frac{Et^3}{12(1 - \nu^2)} (a + u_r)^{3n+1} \left( \frac{d^5 u_r}{dz^5} + \frac{12}{a^2 t^2} \frac{du_r}{dz} \right) = (-2m) \left[ \frac{(3 + 1/n)q}{\pi} \right]^n (1 - \nu^2). \quad (5.14)$$

The dimensionless form of Eq. (5.14), using the variables previously defined in Eq. (4.18), is

$$(1 + \beta\bar{u}_{\bar{r}})^{3n+1} \left[ \underbrace{\left( \frac{t}{a} \right)^2 \left( \frac{a}{\ell} \right)^4 \frac{d^5 \bar{u}_{\bar{r}}}{d\bar{z}^5}}_{\text{bending}} + \underbrace{12 \frac{d\bar{u}_{\bar{r}}}{d\bar{z}}}_{\text{stretching}} \right] = \underbrace{-24(1 - \nu^2)^2 [(3 + 1/n)\bar{q}]^n}_{\text{loading}}. \quad (5.15)$$

The ODE in Eq. (5.15) is subject to the following boundary conditions expressing clamping of the shell at the inlet and outlet planes [Eqs. (5.16a) and (5.16b), respectively] and zero gauge pressure at the outlet [Eq. (5.16c)]:

$$\bar{u}_{\bar{r}}|_{\bar{z}=0} = \frac{d\bar{u}_{\bar{r}}}{d\bar{z}} \Big|_{\bar{z}=0} = 0, \quad (5.16a)$$

$$\bar{u}_{\bar{r}}|_{\bar{z}=1} = \frac{d\bar{u}_{\bar{r}}}{d\bar{z}} \Big|_{\bar{z}=1} = 0, \quad (5.16b)$$

$$\frac{d^4 \bar{u}_{\bar{r}}}{d\bar{z}^4} \Big|_{\bar{z}=1} = 0. \quad (5.16c)$$

Equations (5.15) and (5.16) represent a nonlinear *two-point* (TP) *boundary value problem*

(BVP) (Keller 1976), the solution of which fully characterizes the physics of FSI in microtube conveying a non-Newtonian fluid within.

This theory is based upon the assumptions of slenderness ( $\ell \ll a$ ) and thinness ( $t \ll a$ ). Therefore, in the limit of vanishing  $t/a$  and  $a/\ell$ , Eq. (5.15) becomes an example of a *singular perturbation problem*. Physically, “boundary layers” develop near the inlet and outlet of the microtube where the bending due to clamping becomes significant. As a singular perturbation problem, Eq. (5.15) is now amenable to treatment via *matched asymptotics* (Holmes 2013, Ch. 2).

To that end, we introduce a dimensionless small parameter  $\epsilon = \sqrt{ta/\ell^2} \ll 1$ , then Eq. (5.15) can be rewritten as:

$$(1 + \beta \bar{u}_{\bar{r}})^{3n+1} \left( \epsilon^4 \frac{d^5 \bar{u}_{\bar{r}}}{d\bar{z}^5} + 12 \frac{d\bar{u}_{\bar{r}}}{d\bar{z}} \right) = -24(1 - \nu^2)^2 [(3 + 1/n)\bar{q}]^n. \quad (5.17)$$

As is standard, we first let  $\epsilon \rightarrow 0^+$ , thus singularly perturbing the ODE, and obtain the governing equation for the solution in the *outer region*:

$$(1 + \beta \bar{u}_{\bar{r}})^{3n+1} \frac{d\bar{u}_{\bar{r}}}{d\bar{z}} = -2(1 - \nu^2)^2 [(3 + 1/n)\bar{q}]^n. \quad (5.18)$$

The outer solution must “respect” the first part of the clamping condition at  $\bar{z} = 1$ , i.e.,  $\bar{u}_{\bar{r}}|_{\bar{z}=1} = 0$  from Eq. (5.16b). Then, the solution to the ODE (5.18) is

$$\bar{u}_{\bar{r}}(\bar{z}) = \frac{1}{\beta} \left( \{1 + 2\beta(3n+2)(1 - \nu^2)^2 [(3 + 1/n)\bar{q}]^n (1 - \bar{z})\}^{1/(3n+2)} - 1 \right). \quad (5.19)$$

Note that Eq. (5.19) can also be obtained by combining Eqs. (4.23) and (5.7) from the membrane theory, showing the consistency of our two structural mechanics models.

To satisfy the clamped boundary condition at  $\bar{z} = 0$ , i.e., Eq. (5.16a), we must introduce a *boundary layer* near  $\bar{z} = 0$  wherein the highest-order derivative in Eq. (5.17) is dominant and is retained. Then, an inner solution can be obtained. To this end, we introduce a scaled spatial coordinate  $\zeta$  such that for  $\bar{z} \ll 1$ ,  $\zeta = \mathcal{O}(1)$ . A straightforward balancing argument leads us to define  $\zeta = \bar{z}/\epsilon$ . Then, the nonlinear ODE (5.17) becomes

$$\frac{d^5 \bar{u}_{\bar{r}}}{d\zeta^5} + 12 \frac{d\bar{u}_{\bar{r}}}{d\zeta} = \epsilon \left\{ \frac{-24(1 - \nu^2)^2 [(3 + 1/n)\bar{q}]^n}{(1 + \beta \bar{u}_{\bar{r}})^{3n+1}} \right\}. \quad (5.20)$$

At the leading order in  $\epsilon \ll 1$ , we have

$$\frac{d^5 \bar{u}_{\bar{r}}}{d\zeta^5} + 12 \frac{d\bar{u}_{\bar{r}}}{d\zeta} = 0 \quad (5.21)$$

subject to the following boundary conditions:

$$\bar{u}_{\bar{r}}|_{\zeta=0} = \frac{d\bar{u}_{\bar{r}}}{d\zeta} \Big|_{\zeta=0} = 0, \quad (5.22a)$$

$$\bar{u}_{\bar{r}}|_{\zeta \rightarrow \infty} = \bar{u}_{\bar{r}}^{\text{outer}}|_{\bar{z}=0}, \quad (5.22b)$$

where  $\bar{u}_{\bar{r}}^{\text{outer}}$  denotes the outer solution from Eq. (5.19). Here, the first two boundary conditions (at  $\zeta = 0$ ) are due to clamping, while the remaining boundary condition (as  $\zeta \rightarrow \infty$ ) is necessary to *match* the inner solution to the outer solution.

Next, we integrate Eq. (5.21) once to obtain

$$\frac{d^4 \bar{u}_{\bar{r}}}{d\zeta^4} + 12 \bar{u}_{\bar{r}} = 12C_0, \quad (5.23)$$

where  $C_0$  is a (yet) unknown integration constant. The solution of Eq. (5.23) consists of a homogeneous solution  $\bar{u}_{\bar{r},\text{H}}$  and a particular solution  $\bar{u}_{\bar{r},\text{P}}$ . The homogeneous part of the ODE (5.23) has the characteristic polynomial  $\tau_i^4 = -12$ , the four complex roots of which are easily found, thus

$$\bar{u}_{\bar{r},\text{H}}(\zeta) = C_1 e^{(1+i)\sqrt[4]{3}\zeta} + C_2 e^{-(1+i)\sqrt[4]{3}\zeta} + C_3 e^{(1-i)\sqrt[4]{3}\zeta} + C_4 e^{-(1-i)\sqrt[4]{3}\zeta}. \quad (5.24)$$

Now, since  $\bar{u}_{\bar{r},\text{H}}$  must remain bounded as  $\zeta \rightarrow \infty$ , we require that  $C_1, C_3 = 0$ . The particular solution is easily found to be

$$\bar{u}_{\bar{r},\text{P}}(\zeta) = C_0. \quad (5.25)$$

Before applying the boundary conditions, we redefine the arbitrary constants of integration  $C_1$  and  $C_2$  to be  $\tilde{C}_4 = C_4 + C_2$  and  $\tilde{C}_2 = (C_4 - C_2)i$ . Then, the real-valued general solution,  $\bar{u}_{\bar{r}} = \bar{u}_{\bar{r},\text{H}} + \bar{u}_{\bar{r},\text{P}}$ , to Eq. (5.23) is

$$\bar{u}_{\bar{r}}(\zeta) = e^{-\zeta\sqrt[4]{3}} \left[ \tilde{C}_2 \sin\left(\zeta\sqrt[4]{3}\right) + \tilde{C}_4 \cos\left(\zeta\sqrt[4]{3}\right) \right] + C_0, \quad (5.26)$$

Now, we apply the boundary condition  $\bar{u}_{\bar{r}}|_{\zeta=0} = 0$  to obtain  $\tilde{C}_4 = -C_0$ . Next, we use the boundary condition  $(d\bar{u}_{\bar{r}}/d\zeta)|_{\zeta=0} = 0$  to find that  $\tilde{C}_2 = \tilde{C}_4$ . Finally, from the matching condition in Eq. (5.22b), we find

$$\tilde{C}_4 = \frac{1}{\beta} \left( 1 - \left\{ 1 + 2\beta(3n+2)(1-\nu^2)^2[(3+1/n)\bar{q}]^n \right\}^{1/(3n+2)} \right). \quad (5.27)$$

Thus, the final expression for the inner solution in the boundary layer near  $\bar{z} = 0$  is

$$\bar{u}_{\bar{r}}(\zeta) \sim \tilde{C}_4 \left\{ e^{-\zeta\sqrt[4]{3}} \left[ \sin\left(\zeta\sqrt[4]{3}\right) + \cos\left(\zeta\sqrt[4]{3}\right) \right] - 1 \right\}, \quad (5.28)$$

to the leading order in  $\epsilon$ .

Next, another boundary layer must exist near the outlet at  $\bar{z} = 1$  because, although  $\bar{u}_{\bar{r}}^{\text{outer}} \rightarrow 0$  as  $\bar{z} \rightarrow 1$ ,  $d\bar{u}_{\bar{r}}^{\text{outer}}/d\bar{z} \not\rightarrow 0$  as  $\bar{z} \rightarrow 1$ , i.e., the clamping boundary condition is not fully satisfied. Thus, we expect both the dependent (deformation) and the independent (axial position) variables to be small in this layer. That is, we conjecture that the boundary layer at  $\bar{z} = 1$  is actually a *corner layer* (Holmes 2013, §2.6) (sometimes termed a *derivative layer* (see Neu 2015, pp. 85–93)). As is customary in matched asymptotics, it is our duty now to substantiate this hypothesis. Before we begin, it is also relevant to mention the matched asymptotic solution for a *moving* elasto-hydrodynamic front given in (Elbaz & Gat 2016, §4.2), which it should be noted works somewhat differently in the unsteady problem.

Now, introducing the rescalings  $\zeta = (1 - \bar{z})/\epsilon^{\alpha_1}$  and  $\hat{u}(\zeta) = \bar{u}_{\bar{r}}(\bar{z})/\epsilon^{\alpha_2}$  into Eq. (5.17), we can balance all three terms if and only if  $\alpha_1 = \alpha_2 = 1$ . The first and last terms can be balanced for any  $4 - 5\alpha_1 + \alpha_2 = 0$  as long as  $\alpha_1 < \alpha_2$  but then there is a non-uniqueness of the boundary layer thickness, so we discard this possibility. Then, the nonlinear ODE (5.17) becomes

$$\frac{d^5 \hat{u}}{d\zeta^5} + 12 \frac{d\hat{u}}{d\zeta} = \frac{24(1-\nu^2)^2[(3+1/n)\bar{q}]^n}{(1+\beta\epsilon\hat{u})^{3n+1}}. \quad (5.29)$$

Expanding in  $\epsilon \ll 1$ , we have, at the leading order,

$$\frac{d^5 \hat{u}}{d\zeta^5} + 12 \frac{d\hat{u}}{d\zeta} = 12\mathcal{A}, \quad (5.30)$$

where for convenience we have defined  $\mathcal{A} := 2(1-\nu^2)^2[(3+1/n)\bar{q}]^n$ . The ODE (5.30)



must satisfy the remaining boundary conditions at  $\bar{z} = 1$ , from Eqs. (5.16b) and (5.16c), that are not satisfied by the outer solution, namely

$$\left. \frac{d\hat{u}}{d\zeta} \right|_{\zeta=0} = \left. \frac{d^4\hat{u}}{d\zeta^4} \right|_{\zeta=0} = 0, \quad (5.31a)$$

$$\hat{u}|_{\zeta \rightarrow \infty} = \bar{u}_{\bar{r}}^{\text{outer}}|_{\bar{z}=1}. \quad (5.31b)$$

For a corner layer, the matching condition in Eq. (5.31b) is a bit “trickier” and is implemented using an intermediate variable technique (Holmes 2013, §2.6).

The particular solution of Eq. (5.30) is  $\hat{u}_P = \mathcal{A}\zeta$ . The homogeneous  $\hat{u}_H$  solution of Eq. (5.30) satisfies

$$\frac{d^4\hat{u}_H}{d\zeta^4} + 12\hat{u}_H = 12C_0. \quad (5.32)$$

The solution of the latter ODE, implementing the decay for  $\zeta \rightarrow \infty$ , as above, is

$$\hat{u}_H(\zeta) = e^{-\zeta\sqrt[4]{3}} \left[ \tilde{C}_2 \sin\left(\zeta\sqrt[4]{3}\right) + \tilde{C}_4 \cos\left(\zeta\sqrt[4]{3}\right) \right] + C_0. \quad (5.33)$$

Thus, the general solution to Eq. (5.30) is

$$\hat{u}(\zeta) = e^{-\zeta\sqrt[4]{3}} \left[ \tilde{C}_2 \sin\left(\zeta\sqrt[4]{3}\right) + \tilde{C}_4 \cos\left(\zeta\sqrt[4]{3}\right) \right] + C_0 + \mathcal{A}\zeta. \quad (5.34)$$

Now, we impose the boundary condition  $(d\hat{u}/d\zeta)|_{\zeta=0} = 0$  to find that  $\tilde{C}_2 = \tilde{C}_4 - \mathcal{A}/\sqrt[4]{3}$ . Finally, the boundary condition  $(d^4\hat{u}/d\zeta^4)|_{\zeta=0} = 0$  requires that  $\tilde{C}_4 = 0$ . Thus, we have obtained a fully-specified corner layer (inner) solution:

$$\hat{u}(\zeta) \sim \mathcal{A} \left[ \zeta - \frac{e^{-\zeta\sqrt[4]{3}}}{\sqrt[4]{3}} \sin\left(\zeta\sqrt[4]{3}\right) \right] + C_0. \quad (5.35)$$

The inner solution in Eq. (5.35) must still be matched to the outer solution in Eq. (5.19), which goes to zero as  $\bar{z} \rightarrow 1$ . Thus, we immediately conclude that  $C_0 = 0$ , and the common part of the inner and outer solutions is  $\mathcal{A}\zeta$  [as can be confirmed by a Taylor series expansion of Eq. (5.19) for  $\bar{z} \approx 1$ ]. This argument can be made even more rigorous using an intermediate variable matching procedure as in (Holmes 2013, §2.6).

Finally, adding together Eqs. (5.19), (5.28) and (5.35) (expressed in the original variables) and subtracting their mutual common parts, we obtain a *composite solution* uniformly valid on  $\bar{z} \in [0, 1]$ , to the leading order in  $\epsilon$ :

$$\begin{aligned} \bar{u}_{\bar{r}}(\bar{z}) \sim & \frac{1}{\beta} \left( \left\{ 1 + 2\beta(3n+2)(1-\nu^2)^2[(3+1/n)\bar{q}]^n(1-\bar{z}) \right\}^{1/(3n+2)} - 1 \right) \\ & + \tilde{C}_4 e^{-\sqrt[4]{3}\bar{z}/\epsilon} \left[ \sin\left(\sqrt[4]{3}\frac{\bar{z}}{\epsilon}\right) + \cos\left(\sqrt[4]{3}\frac{\bar{z}}{\epsilon}\right) \right] \\ & - \epsilon \frac{2(1-\nu^2)^2[(3+1/n)\bar{q}]^n}{\sqrt[4]{3}} e^{-\sqrt[4]{3}(1-\bar{z})/\epsilon} \sin\left(\sqrt[4]{3}\frac{(1-\bar{z})}{\epsilon}\right), \end{aligned} \quad (5.36)$$

where the constant  $\tilde{C}_4$  is given in Eq. (5.27).

REMARK 6. Čanić & Mikelić (2003) discussed the formation of deformation “boundary layers” in the context of viscous incompressible flow through a long elastic tube, as the aspect ratio  $a/\ell \rightarrow 0^+$ . Their approach was based on a priori estimates of the coupled PDEs. Here, we have actually constructed the boundary (and corner) layers explicitly through a matched asymptotic expansion, further showing that the relevant small parameter also involves the microtube’s thickness:  $\epsilon = \sqrt{ta/\ell^2}$ . Our result, then, is closer

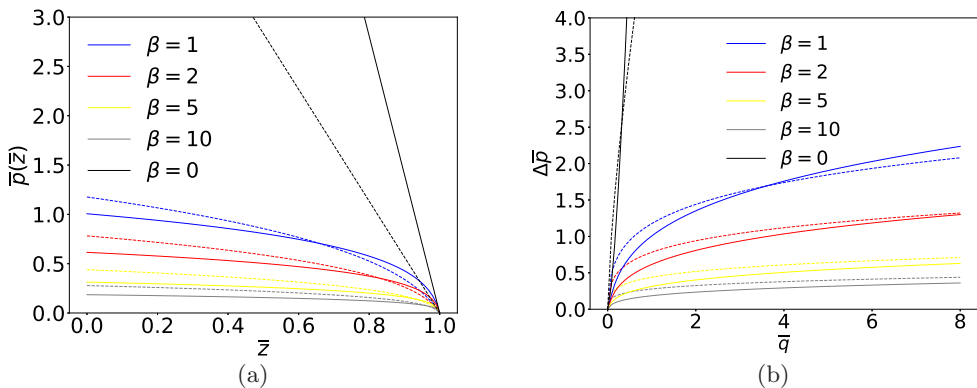


FIGURE 2. (a) The dimensionless hydrodynamic pressure  $\bar{p}$  in a microtube as a function of the dimensionless axial coordinate  $\bar{z}$  for different values of the FSI parameter  $\beta$  with  $\bar{q} = 1$ . (b) Full dimensionless pressure drop  $\Delta\bar{p}$  across a microtube as a function of the dimensionless flow rate  $\bar{q}$  for different values of  $\beta$ . Both plots have been produced using Eq. (5.7). The dashed and solid curves represent a shear-thinning ( $n = 0.7$ ) and a shear-thickening fluid ( $n = 1.5$ ), respectively. Note the different vertical scales in panels (a) and (b).

to some of the discussion in textbooks on shell theory, wherein the (dimensional) thickness of boundary layers (near the clamped ends of a Donnell shell subject to uniform internal pressure) is estimated to be  $\mathcal{O}(\sqrt{ta})$  (see Dym 1990, Ch. V).

## 6. Results and discussion

### 6.1. Deviations from the Hagen–Poiseuille law due to FSI

Our objective is to understand and quantify the deviation, caused by FSI in a microtube, from the Hagen–Poiseuille law. To this end, we must evaluate the effects of two competing physical mechanisms: (i) the non-Newtonian rheology of the fluid (quantified by its power-law index  $n$ ), and (ii) the compliance of the microtube’s wall (quantified by the FSI parameter  $\beta$ ). On one hand, the viscous stresses in the fluid and its flow resistance increase with  $n$ , which leads to a larger pressure drop at a fixed inlet flow rate. On the other hand, the effective cross-sectional area of the flow conduit increases with  $\beta$  (stronger FSI/more deformation), thereby reducing the resistance to flow and the concomitant pressure drop. Thus, there is a non-trivial interplay of shear-dependent viscosity and tube wall compliance, as we now discuss (and as is further elucidated in Appendix B).

First, consider Fig. 2(a), which shows the pressure profile,  $\bar{p}(\bar{z})$ , along the length of the microtube. We immediately recognize that, due to FSI and non-Newtonian rheology, the pressure profile is not linear in  $\bar{z}$ . Overall, the maximum pressure in the presence of non-Newtonian FSI ( $\beta \neq 0$  and  $n \neq 1$ ) is *significantly* reduced compared to flow in a rigid tube ( $\beta = 0$ , black curves).

Next, Fig. 2(b) shows the full (dimensionless) pressure drop  $\Delta\bar{p}$  as a function of the flow rate  $\bar{q}$  for different values of  $\beta$ . At flow rates  $\bar{q} \gtrsim 3$ ,  $\Delta\bar{p}$  is larger for shear-thickening fluids (solid curves,  $n > 1$ ) for the smallest value of  $\beta = 1$  shown, but order trend is *counterintuitively* reversed at large  $\beta$  values, and the shear-thinning fluids (dashed curves,  $n < 1$ ) exhibit a larger  $\Delta\bar{p}$ . This observation is clearly a manifestation of the competition of physical effects mentioned above. Also, note that the flow rate–pressure

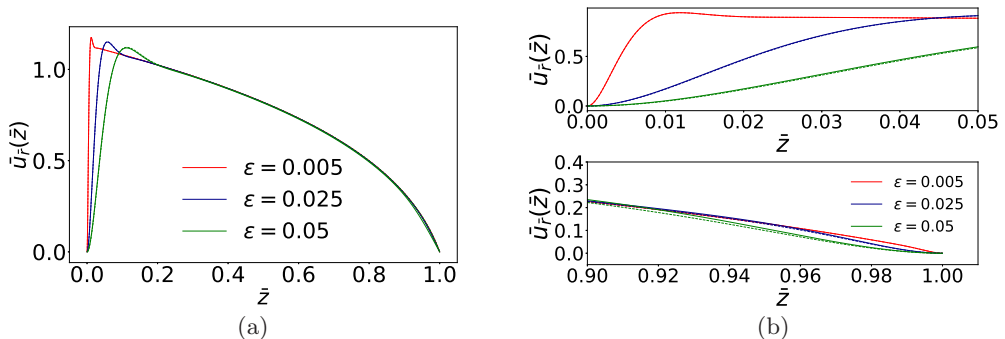


FIGURE 3. The dimensionless radial displacement  $\bar{u}_r(\bar{z})$  as a function of the dimensionless axial position  $\bar{z}$  in the microtube for  $\beta = 1$ ,  $n = 0.7$ ,  $\bar{q} = 2$  and  $\nu = 1/2$ . The solid curves are the numerical solution of TPBVP given by Eqs. (5.15) and (5.16), while dashed curves are the matched asymptotic solution, namely Eq. (5.36). Panel (a) shows the displacement over the whole tube, while panels (b) and (c) show zoom-ins near the clamped ends. In most cases the agreement between the numerical and asymptotic solutions is so good that they are difficult to distinguish.

drop relation is nonlinear for power-law fluids even for rigid walls ( $\beta = 0$ , black curves), as is well established in textbooks (Bird *et al.* 1987). This result is also contained in Eq. (5.4), even if it is not so obvious due to the scales in Fig. 2(b). Once again, we conclude by noting that  $\Delta\bar{p}$  is *very significantly* reduced by FSI.

### 6.2. Comparison between the analytical and numerical solutions of theory

Our results in §5, suggest the following possible ways for solving the coupled problem of flow and deformation in an elastic tube: (i) using leading-order-in-thickness membrane theory (§5.2), (ii) using a matched asymptotic expansion for beyond-leading-order-in-thickness (i.e., Donnell shell) theory to capture bending and clamping (§5.3), and (iii) by numerical integration of the nonlinear ODE (5.15) for the displacement. We may conceptualize these approaches as a hierarchy: the leading-order perturbative solution is a less accurate version of the solution obtained by the matched asymptotic expansion, while the matched asymptotic expansion is a less accurate version of the solution found by numerically integrating the ODE.

Let us now compare the deformation profile obtained via matched asymptotic expansion, i.e., Eq. (5.36) to the numerical solution of the original nonlinear TPBVP, i.e., Eqs. (5.15) and (5.16). The latter profile is obtained by using the `solve_bvp` method in Python’s SciPy module (Jones *et al.* 2001) to solve the TPBVP numerically. Figure 3 shows the results of such a comparison for different values of the small parameter  $\epsilon = \sqrt{ta}/\ell^2$  but fixed  $\beta$ ,  $n$ ,  $\bar{q}$  and  $\nu$ . There is very good agreement between the composite solution obtained via a matched asymptotic expansion and the numerical solution of the nonlinear TPBVP. As expected, the error in the composite solution increase with  $\epsilon$ , especially in the corner layer at  $\bar{z} = 1$ , nevertheless the asymptotic expression is clearly very accurate.

In addition, observe that the axial displacement profile exhibits an overshoot near the inlet due to clamping, which is not the case for a two-dimensional plate top wall in a soft microchannel (Christov *et al.* 2018; Shidhore & Christov 2018; Anand *et al.* 2019). This complex feature of the displacement profile, along with the corner layer at the outlet, are accurately captured by the matched asymptotic solution given in Eq. (5.36).

---

$a$ (mm)	$\ell$ (mm)	$a/\ell$	$t$ (mm)	$t/a$	$E$ (MPa)	$\nu$	$\mu$ (Pa·s)	$n$	$m$ (Pa·s <sup><math>n</math></sup> )	$\rho$ (kg/m <sup>3</sup> )
0.08	3.2	0.025	0.008	0.1	0.5	0.499	0.0012	0.7	0.0185	1060

---

TABLE 1. Geometric and material properties for a sample microtube FSI problem.

### 6.3. Comparison between theory and direct numerical simulations

To ascertain the validity of the theory developed in this paper, we now compare our theoretical results against 3D direct numerical simulations (DNS) of coupled flow and deformation in a microtube. To this end, we choose an illustrative set of physical and geometric parameters, given in Table 1. The microtube is assumed to be made of elastin, which is a highly elastic protein found in all vertebrates and is major constituent of arteries (Sandberg *et al.* 1977). Here, along the lines of the work in (Sandberg *et al.* 1977; Matsumoto *et al.* 2015; Ebrahimi 2009), elastin is modeled as an isotropic linearly elastic solid with a constant Young’s modulus of  $E = 0.5$  MPa and a Poisson ratio of  $\nu = 0.499$  (i.e., a nearly incompressible material, consistent with the discussion in §4.1). The dimensions have been chosen to ensure that the assumptions of shallowness and slenderness are satisfied. Specifically, the thickness-to-radius ratio of the microtube is fixed at  $t/a = 0.1$ , consistent with the hemodynamics literature (Vlachopoulos *et al.* 2011, p. 60). The radius-to-length ratio is chosen to be sufficiently smaller,  $a/\ell = 0.025 \ll t/a$ , and the length  $\ell = 3.2$  mm is chosen to be similar to microchannel studies (see, e.g., Shidhore & Christov 2018), from which the values of  $a$  and  $t$  in Table 1 follow.

The generalized Newtonian fluid inside the microtube is assumed to be human blood. Blood rheology is a topic of active research, as the rheological properties of blood depend on various factors such as a patient’s age, health, concentration of plasma, etc. (Hussain *et al.* 1999; Chakraborty 2005). Here, for the sake of simplicity, and without sacrificing any physics, and to validate our theory for both Newtonian and non-Newtonian rheology, blood plasma is chosen as our example of Newtonian fluid with constant shear viscosity of  $\mu = 0.0012$  Pa·s (i.e.,  $m = \mu$  and  $n = 1$ ) (Fung 1997), while whole blood is chosen as our example shear-thinning fluid with a power-law index of  $n = 0.7$  and a consistency index of  $m = 0.0185$  Pa·s <sup>$n$</sup>  (Hussain *et al.* 1999). In both cases, a density of  $\rho = 1060$  kg/m<sup>3</sup> is used, which is within the range for both blood plasma and whole blood (see, e.g., Kleinstreuer 2006, Table 2.1.1). Simulations were carried out for flow rates up to  $q = 2.00$  mL/min, which corresponds to a maximum  $Re \approx 150$  and a maximum FSI parameter  $\beta \approx 0.12$ .

For our computational approach, we employ a segregated solution strategy, as opposed to a monolithic one (see, e.g., Bazilevs *et al.* 2013). That is, the solid (resp. fluid) problem is solved independently of the fluid (resp. solid) problem, each on its own computational domain. The displacements (resp. forces) from the solid (resp. fluid) domain are then transferred to the fluid (resp. solid) domain via a surface traction boundary condition. Based on previous successful computational microscale FSI studies (Chakraborty *et al.* 2012; Shidhore & Christov 2018; Anand *et al.* 2019), we have used the commercial computer-aided engineering (CAE) software from ANSYS Inc. (2018) to perform such two-way coupled FSI DNS via a segregated approach. The geometry was created in ANSYS SpaceClaim, and the mesh was generated in ANSYS ICEM CFD. The steady incompressible mass and momentum equations for the power-law fluid were solved using ANSYS Fluent as the computational fluid dynamics (CFD) solver based on the finite volume method. The structural mechanics solver, based on the finite element method (FEM), under ANSYS Mechanical was employed for the structural

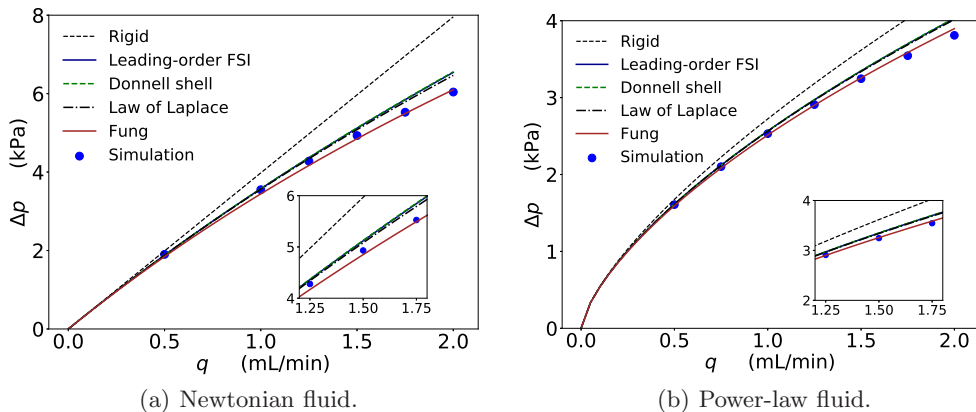


FIGURE 4. Pressure drop vs. flow rate in a deformable microtube. Fluid–structure interaction causes the pressure drop to decrease in the deformable tube compared to the rigid one. The perturbative analysis developed herein, culminating in Eqs. (5.8) [power-law, (b)] and (5.12) [Newtonian, (a)] captures the latter effect quite accurately, when compared to 3D direct numerical simulations. The leading-order FSI, the Donnell shell FSI and the large-deformation leading-order FSI curves are nearly identical in both panels. Note the different vertical scales in panels (a) and (b).

problem, which solved the static force-equilibrium equations for a linearly elastic isotropic solid with geometrically nonlinear strains. The exchange of forces and displacements along the inner surface of the tube was performed by declaring the surface as an ‘FSI interface.’ A nonlinear iterative procedure transfers the loads and displacements incrementally until convergence is reached, ensuring a full two-way coupling. Most importantly, beyond assuming a steady state, this DNS approach *does not* make any of the approximations that the theory does, e.g., lubrication, Donnell shell, and the various smallness assumptions.

### 6.3.1. Fluid mechanics results

First, we benchmark the  $q$ – $\Delta p$  relationships predicted by our mathematical models: the leading-order FSI from the membrane theory [Eq. (5.8)] and the Donnell shell FSI [Eqs. (4.17) and (5.14)]. The dimensional full pressure drop  $\Delta p$  as a function of the dimensional flow rate  $q$  is shown in Fig. 4 for (a) a Newtonian fluid (blood plasma) and (b) a shear-thinning fluid (whole blood). There is good agreement between theory and simulation, particularly for the smaller flow rates. The maximum relative error, over shown range of  $q$ , is  $\approx 10\%$  for the Newtonian fluid and  $\approx 5\%$  for the shear-thinning fluid. At larger  $q$ , small but systematic differences emerge between theory and simulation because, at these flow rates, the deformation of the microtube starts to exhibit significant strains, which are beyond the applicability of the linear shell theory employed herein. We also observe that there is hardly any perceptible difference in  $\Delta p$  predicted by the membrane and Donnell shell theories, which shows that bending is indeed negligible when computing the pressure drop.

It is important to evaluate the theory developed herein in the context of the classical results, namely the law of Laplace (Čanić *et al.* 2006, 2007) and the model proposed by Fung in his *Biomechanics* textbook (Fung 1997, §3.4), which is often quoted in newer texts on biofluid mechanics (Ayyaswamy 2016, pp. e25–e27). Fung’s model and that of Laplace take a large-deformation approach, writing the stress equilibrium equations in

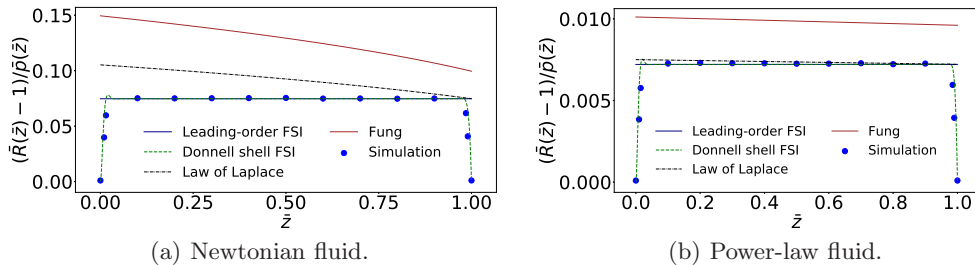


FIGURE 5. Ratio of the dimensionless radial deformation  $\bar{R} - 1$  to the hydrodynamic pressure  $\bar{p}$ , as a function of the axial position  $\bar{z}$  in the microtube. The leading-order FSI theory is given by Eq. (4.23), the Donnell shell FSI theory is the numerical solution of the TPBVP given by Eqs. (5.15) and (5.16), the law of Laplace is given by Eq. (C 4), Fung’s result is given by Eq. (C 4) with  $\nu = 0$ , and the simulation results are from ANSYS.

the *deformed* configuration of the microtube. To this end, in Appendix C, we have also re-derived our main mathematical result [i.e., Eq. (5.6)] in this large-deformation context. Thus, in Fig. 4, we can compare the results of the Fung’s theory and the law of Laplace, alongside those of our leading-order (membrane) and Donnell-shell FSI theories. The pressure drops predicted by the different mathematical theories considered are quite close. While Fung’s model first overpredicts then underpredicts the pressure drop, the other theories over-predict the pressure drop with increasing error as  $q$  increases, consistent with the perturbation approach under which they were derived. As expected, given the small deformation of the microtube, a large-deformation membrane theory does not produce much of a difference. Based on the discussion in Appendix C, we must conclude that the assumptions about the deformation and the stress fields (see below) made in Fung’s classic treatment of the problem *coincidentally* yields good agreement at large  $q$ , while it reduces to the theory derived herein for small  $q$ .

### 6.3.2. Structural mechanics results

Having compared and verified the theoretical prediction for the hydrodynamics portion of the FSI problem, we now shift our focus to the solid domain. In Fig. 5, we plot the ratio of dimensionless radial tube deformation,  $\bar{R}(\bar{z}) - 1$ , to the dimensionless pressure  $\bar{p}(\bar{z})$  along the microtube’s length. Again, the results have been shown for both our chosen (a) Newtonian and (b) shear-thinning fluid. Equations (4.22) and (4.23) predict this ratio to be  $[\bar{R}(\bar{z}) - 1]/\bar{p}(\bar{z}) = \beta(1 - \nu^2)$  (interestingly, a constant independent of  $\bar{z}$ ), to the leading order in  $\epsilon = \sqrt{ta/\ell^2}$ . For the beyond-leading-order analysis, we integrated the fifth-order nonlinear BVP from Donnell’s shell theory, i.e., Eq. (5.15) subject to Eqs. (5.16), using the TPBVP solver method in Python’s SciPy module (Jones *et al.* 2001). (We could have also plotted the matched asymptotic solution to Eq. (5.15), namely Eq. (5.36), but it would be indistinguishable for this value of  $\epsilon = 6.25 \times 10^{-5}$  based on Table 1.)

Figure 5 shows good agreement between the results of DNS and the two mathematical models developed in this paper, namely the leading-order FSI and the Donnell shell FSI. Additionally, the conflicting assumptions used to obtain the law of Laplace and Fung’s result are quite apparent in this comparison. For both Newtonian and power-law fluid, Fung’s model significantly overpredicts this ratio. As explained in more detail in Appendix C, Fung’s model is an “independent ring” model that neglects the stress and strains in the axial (flow-wise) direction. These assumptions, in conjunction with those of large-deformation FSI, lead both Fung’s model and the law of Laplace to predict an

incorrect displacement profile for which  $[\bar{R}(\bar{z}) - 1]/\bar{p}(\bar{z})$  slowly varies with  $z$  (outside the boundary and corner layers).

Perhaps more interestingly, there is an extremely narrow region near the inlet ( $\bar{z} = 0$ ) and outlet ( $\bar{z} = 1$ ) planes, wherein the full ODE solution deviates from the leading-order perturbative solution; these are “boundary layers” discussed in §5.3. The thinness of these boundary layers, in comparison with the tube’s length, leads us to conclude that almost the entire tube, except a sliver near each end, is in a membrane state with negligible bending.

#### 6.4. Region of validity in the parameter space

The theory of non-Newtonian FSI in microtubes developed herein hinges upon certain key assumptions. Thus, to complete our discussion, it is imperative to mention when the assumptions in our theory are valid, i.e., for what choices of the physical and geometric parameters does our theory accurately capture FSIs in microtubes. For example, even at vanishing Reynolds number, microtube FSI can lead to buckling of the elastic structure and collapse of the flow passage (Heil 1997), which is beyond the scope of our theory.

Thus, for our linear, small-deformation FSI theory to hold true, we must require that

- (i)  $t/a \ll 1$ : This assumption allows us to use thin-shell theory.
- (ii)  $\mathcal{U}_c/a \ll 1$ : This is the small-strain assumption of the shell theory.
- (iii)  $a/\ell \ll 1$ : This slender-geometry assumption allows us to simplify both the fluid mechanics and the structural mechanics problems. This assumption also ensures the rotation of a shell element is negligible.
- (iv)  $\mathcal{U}_c/t \ll 1$ : This assumption allows us to refer the analysis to the undeformed (Eulerian) coordinates. This assumption also restricts the current theory to small deformations.

A natural ordering of the physical dimensions of the tubes thus follows:

$$\mathcal{U}_c \ll t \ll a \ll \ell, \quad (6.1)$$

which must hold for the present linear, small-deformation FSI theory to apply. Importantly, our DNS results show that this regime is accessible under realistic flow conditions.

## 7. Conclusions and outlook

In this paper, we have formulated a theory of the axisymmetric fluid–structure interaction (FSI) between a generalized Newtonian fluid and a deformable circular cylinder at the microscale. Specifically, we have derived an analytical expression relating the pressure drop across the microtube to the imposed steady flow rate through it, taking into account both the fluid’s shear-dependent viscosity (such as, e.g., whole blood) and the compliance of the conduit (such as, e.g., a blood vessel). Although physiological flows occur across a range of flow regimes (Reynolds numbers) (Pedley 1980; Grotberg 1994; Grotberg & Jensen 2004; Heil & Hazel 2011), previous research has focused on moderate-to-high Reynolds number phenomena, including collapse of the vessel, unlike the present context of low Reynolds number steady FSI. The proposed theory is also applicable to problems in microfluidics, wherein soft (PDMS-based) microchannels of circular cross-section are now manufactured and FSI becomes relevant (Paek *et al.* 2015; Raj M *et al.* 2018).

Under the lubrication approximation for low Reynolds number flow, we showed how to analytically couple a unidirectional flow field to an appropriate linear shell theory. This led us to a fifth-order nonlinear ordinary differential equation (ODE) for the radial displacement, namely Eq. (5.15), that fully describes the FSI. In a perturbative sense,

we showed that, at the leading order in slenderness and shallowness of the tube, the shell theory reduces to membrane theory and a *linear* relationship, namely Eq. (4.23), emerges between the local radial deformation and the local hydrodynamic pressure at a given cross-section. Then, a “generalized Poiseuille law” was obtained, namely Eq. (5.8), *explicitly* relating the pressure drop to the imposed flow rate. This relationship rationalizes and updates certain heuristic arguments often found in textbook discussion of physiological flow (Fung 1997; Ayyaswamy 2016). Specifically, Eq. (5.12) can be put into dimensional form to yield the pressure drop for flow of a Newtonian fluid in a slender deformable tube:

$$\Delta p = \frac{Et}{(1-\nu^2)a} \left\{ \left[ 1 + 40(1-\nu^2) \frac{\mu q \ell}{Et\pi a^3} \right]^{1/5} - 1 \right\}. \quad (7.1)$$

The most important observation is that Eq. (7.1) is *nonlinear* in  $q$  (due to FSI), even for a Newtonian fluid (in stark contrast to the Hagen–Poiseuille law).

Furthermore, we showed that a boundary layer (at the inlet) and a corner layer (at the outlet) of the microtube are required to enforce the clamping conditions on the structure. Using the method of matched asymptotics, we obtained a uniformly valid (closed-form) expression for a deformation profile, namely Eq. (5.36). The ability to solve for the microtube’s deformation as a function of the axial coordinate via a matched-asymptotics calculation is in stark contrast with the case of low Reynolds number FSI in a microchannel of rectangular cross-section (Christov *et al.* 2018; Anand *et al.* 2019) (see also §7.1).

To ascertain the validity of our mathematical results, we specified, through Eq. (6.1), the region in the (vast) FSI parameter space in which our theory applies. Then, we carried out two-way-coupled 3D simulations using the commercial computer-aided engineering suite by ANSYS Inc. (2018). We showed that good agreement can be obtained between predictions from the theory (for both the pressure drop and the radial deformation) and the corresponding direct numerical simulations.

A counterintuitive result stemming from this work is that, due to the complex interplay between FSI and fluid rheology, certain shear-*thickening* fluids flow more easily (i.e., require lower  $\Delta p$  to maintain a constant  $q$ ) than certain shear-*thinning* fluids. This effect is observed for “stronger” FSI (i.e., the dimensionless FSI parameter  $\beta \gg 1$ ). This anomalous enhancement should be interrogated experimentally due to its potential use in lab-on-a-chip technologies.

In future work, the FSI theory developed herein can be extended to incorporate further physical effects that arise in microscale fluid mechanics. For example, the material composing the tube may not be only elastic but also porous (i.e., *poroelastic*) (Auton & MacMinn 2017). It may also be worthwhile to consider microflows of gases in elastic tubes, which necessitates accounting for compressibility of the fluid (Elbaz *et al.* 2018) and possible wall slip (San & Staples 2012). Another potential avenue for future research stems from the fact that many soft biological tissues are *hyperelastic*. In this case, the stress–strain relationship is obtained from extremizing a prescribed strain-energy functional (see, e.g., Fung 1993, Ch. 8 and 9). With such an elastic response in hand, the microtube FSI problem considered herein can be generalized, along the lines of Anand & Christov (2019), who considered only leading-order (in the present terminology) hyperelastic FSI.



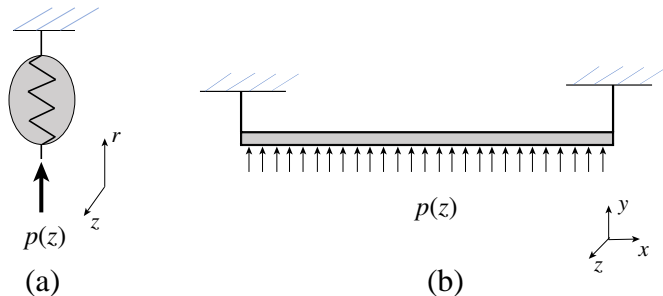


FIGURE 6. (a) A slice of a soft microtube represented as a Hookean spring. (b) A slice of a microchannel’s soft top wall represented as an Euler beam. Both are uniformly loaded but the hydrodynamic pressure  $p$  at flow-wise cross-section  $z$ .

### 7.1. Comparison to viscous FSI in a rectangular microchannel: Plates vs. shells

As mentioned previously, the deformation of any slice of the soft microtube considered herein is akin to a Hookean spring because of the direct *linear* proportionality between the deformation and the pressure expressed by Eq. (4.23). The deformation of any infinitesimal slice in the flow-wise direction is independent of the deformation of neighboring slices, just as for a slender microchannel with a soft top wall (Christov *et al.* 2018; Shidhore & Christov 2018; Anand *et al.* 2019). The mathematical reason for this decoupling is the same for both geometries: the flow-wise length scale of the microtube/channel is much larger than its cross-sectional dimension. However, the two cases should also be contrasted: for a long and shallow microchannel, each slice of the top wall acts like an Euler beam in the cross-sectional direction (due to clamping at the sidewalls). Meanwhile, for a slender microtube, each slice acts as a Hookean spring (due to axisymmetric deformation), as illustrated schematically in Fig. 6. Consequently, it is easy to intuit why a microtube is more compliant (and thus deforms more than a similar microchannel), with all other conditions being the same. This result is connected to the fact that for the microchannel, only the top wall is deformable, while the full circumference of the microtube is deformable.

We thank T. C. Shidhore for assistance with the initial forays into two-way ANSYS FSI simulations of microtubes and advice related to the latter, and X. Wang for a careful reading of the manuscript. This research was supported by the US National Science Foundation under grant No. CBET-1705637.

## Appendix A. Grid-independence study

To ensure that the numerical solution that we computed is independent of mesh size, we performed a grid independence study. Two grids each were defined for the fluid and the solid solvers, respectively, thus bringing the total number of grid arrangements to four. The details of the grids are shown in Table 2. For the fluid mesh, grid 2 was generated by scaling the number of edge divisions across the model in grid 1 by a factor of 2. Similarly, grid 2 for the FEM mesh was generated by increasing the number of divisions on the lateral surfaces from 500 to 800. On all four grids, the simulations were performed for the fluid and solid models describe above, under the conditions in Table 1. However, for the grid refinement study, the simulations were carried out only for a single flow rate of  $q = 1$  mL/min.

The results of the grid convergence study are shown in Table 3 for the average

---

	fluid mesh 1	fluid grid 2	solid mesh 1	solid mesh 2
Number of nodes	1 348 768	10 626 967	1 090 584	1 743 984
Number of elements	1 387 365	10 467 576	198 000	316 800

---

TABLE 2. Details for the four meshes used for the grid-convergence study.

---

fluid mesh/solid mesh	1/1	2/1	1/2	2/2
$\langle u_r \rangle$ % difference	0.2	-0.4	-0.6	-
$\Delta p$ % difference	-0.08	0.08	0.04	-

---

TABLE 3. Grid-convergence (mesh-independence) study for the microtube simulations above using the circumferentially averaged displacement  $\langle u_r \rangle$  at the tube wall's midsection and the full pressure drop  $\Delta p$  as the metrics. The percent difference is computed with respect to the reference values from the simulation on the combination of fluid mesh 2 and solid mesh 2.

displacement over the circumference at the midsection of the tube and the pressure drop over the length of the microtube. The insignificant variation of these values across grid combinations shows that our simulation results, which were computed on the combination fluid mesh 1 and solid mesh 1, are indeed grid independent and accurate.

## Appendix B. Interplay between $\beta$ and $n$ and its effect on the pressure

The FSI parameter  $\beta$  and the power-law index  $n$  tend to have an opposite effect to each other on the pressure drop across the microtube, as highlighted in §6.1. While  $\beta$  tends to reduce the pressure drop by allowing the flow to pass through a larger area, an increase in  $n$  leads to higher pressure drops via increased resistance to flow. Which of these effects dominates, depends on the values of  $\beta$  and  $n$ . To understand this point, we differentiate the full pressure drop  $\Delta \bar{p}$ , computed from Eq. (5.7), with respect to  $n$  to obtain

$$\begin{aligned} \frac{\partial \Delta \bar{p}}{\partial n} = & \frac{1}{\beta(1-\nu^2)(2+3n)^2} \left( \left[ 1 + 2(3+1/n)^n(2+3n)\beta(1-\nu^2)\bar{q}^n \right]^{1/(2+3n)} \right. \\ & \times 2\beta(1-\nu^2)(3+1/n)^n(2+3n) \\ & \times \bar{q}^n \left\{ \frac{[1+6n+(2+9n(1+n))\ln(3+1/n)+(2+9n(1+n))\ln\bar{q}]}{1+3n+2\beta(1-\nu^2)(3+1/n)^n(2+9n(1+n))\bar{q}^n} \right\} \\ & \left. - 3\ln[1+2\beta(1-\nu^2)(3+1/n)^n(2+3n)\bar{q}^n] \right). \quad (\text{B1}) \end{aligned}$$

The expression from, Eq. (B1) is plotted as a function of  $\beta$  and  $n$  in Fig. 7 for (a)  $\bar{q} = 1$  and (b)  $\bar{q} = 3$ , which shows that  $\partial \Delta \bar{p} / \partial n$  is negative, except for small  $\beta$  (weak FSI). Figure 7 further confirms our earlier observation (from §6.1) that for  $\beta \ll 1$ ,  $\Delta \bar{p}$  increases with  $n$ , but this trend is reversed for larger  $\beta$ , for which  $\Delta \bar{p}$  decreases with  $n$ .

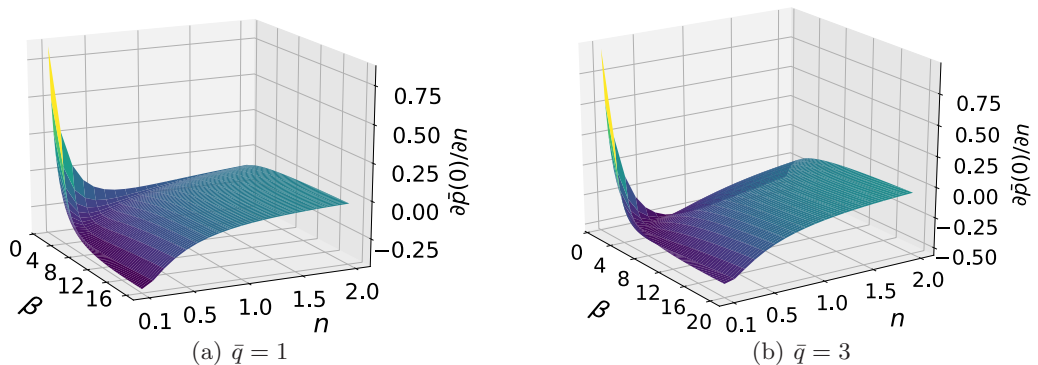


FIGURE 7.  $\partial\Delta\bar{p}/\partial n$  as a function of  $\beta$  and  $n$  for (a)  $\bar{q} = 1$  and (b)  $\bar{q} = 3$ . Both plots show that  $\partial\Delta\bar{p}/\partial n$  is negative, i.e.,  $\Delta\bar{p}$  decreases with  $n$ , except for  $\beta \ll 1$ .

### Appendix C. Large-deformation formulation and connections to Fung’s theory and the law of Laplace

In §4, we termed the proposed FSI theory as *small deformation* due to our assumptions on the structural mechanics aspect of the FSI. We used small-deformation classical shell theories, which assume that the (radial) deformation is considerably smaller than the (smallest) characteristic dimension of the tube, i.e.,  $U_c/t \ll 1$ . This assumption ensures the equivalence between the deformed and undeformed coordinates (i.e., between the Eulerian and Lagrangian frames). Then, the equations of static equilibrium, which are strictly valid only when written in terms of deformed coordinates, can be written in terms of the undeformed coordinates, as done above and in classical shell theory. However, some prior work in the literature has used a mixture of frames of references by posing the equilibrium equations of a small-deformation shell theory in the deformed configuration, while using the equivalence of frames in the subsequent calculation of deformations from strains. Thus, in this appendix, we offer a critical discussion of this issue. The resulting theory may be termed “large-deformation” theory.

The membrane theory of §4.1, when referred to the tube’s deformed coordinates, leads to the following relations expressing the static equilibrium and the stress:

$$N_\theta = R(z)p \quad \Rightarrow \quad \sigma_{\theta\theta} = \left[ \frac{R(z)}{t} \right] p, \quad (\text{C } 1a, b)$$

in analogy to Eqs. (4.3) and (4.4). The assumption of no axial displacement leads to Eq. (4.2), whence the hoop strain (found using the linear elastic law) is  $\varepsilon_{\theta\theta} = (1 - \nu^2)\sigma_{\theta\theta}/E$ , and the concomitant radial deformation is given by

$$u_r(z) = \varepsilon_{\theta\theta}a = (1 - \nu^2) \frac{R(z)a}{Et} p(z). \quad (\text{C } 2)$$

Equation (C 2) is the so-called *law of Laplace*, which relates the pressure at a given cross-section to its radius in the *deformed* state (Čanić *et al.* 2006, 2007). This result, in mixing frames of reference without rigorous motivation for doing so, is not without criticism in the biomechanics literature (Costanzo & Brasseur 2015). Furthermore, observe that  $u_r$  appears on both sides of Eq. (C 2) because  $R(z) = a + u_r(z)$ .

Using the dimensionless variables from Eq. (4.18), Eq. (C 2) becomes

$$U_c \bar{u}_{\bar{r}}(\bar{z}) = (1 - \nu^2) \frac{(a + U_c \bar{u}_{\bar{r}})a}{Et} \mathcal{P}_c \bar{p}(\bar{z}). \quad (\text{C } 3)$$

Now, for large deformations, the appropriate scale is  $\mathcal{U}_c = t$ , which ensures consistency with the results above by keeping the FSI parameter defined as  $\beta = \mathcal{P}_c a / (Et)$ . Thus, solving for  $\bar{u}_{\bar{r}}$  from Eq. (C3), we obtain the pressure–deformation relationship:

$$\bar{u}_{\bar{r}}(\bar{z}) = \left[ \frac{(1 - \nu^2)\beta\bar{p}(\bar{z})}{1 - (1 - \nu^2)\beta\bar{p}(\bar{z})} \right] \left( \frac{a}{t} \right). \quad (\text{C4})$$

Note that, unlike the case of small-deformation theory leading to Eq. (4.23), this last relationship between deformation and pressure is not linear in  $p(z)$ .

Next, we substitute  $\bar{R}(\bar{z}) = 1 + (t/a)\bar{u}_{\bar{r}}(\bar{z})$  and Eq. (C4) into Eq. (5.2) (the flow rate–pressure gradient relationship) an ODE in for the pressure  $\bar{p}(\bar{z})$ , and solve it subject to the outlet pressure BC,  $\bar{p}(1) = 0$ , to yield

$$\bar{p}(\bar{z}) = \frac{1}{(1 - \nu^2)\beta} \left( 1 - \left\{ 1 + 6n(1 - \nu^2)\beta[(3 + 1/n)\bar{q}]^n(1 - \bar{z}) \right\}^{-1/3n} \right). \quad (\text{C5})$$

Setting  $\bar{p}(0) = \Delta\bar{p}$ , the flow rate–pressure drop relation is

$$\bar{q} = \left\{ \frac{[1 - (1 - \nu^2)\beta\Delta\bar{p}]^{-3n} - 1}{6n(3 + 1/n)^n(1 - \nu^2)\beta} \right\}^{1/n}. \quad (\text{C6})$$

In §6.3 (Fig. 4), it was shown that this flow rate–pressure drop relationship based on the law of Laplace is almost indistinguishable from the corresponding one obtained from small-deformation theory, namely Eq. (5.8). To justify this observation mathematically, we perform a Taylor series expansion of Eq. (C6) for  $\beta \ll 1$ , which leads to

$$\bar{q}^n = \frac{1}{2(3 + 1/n)^n} \left\{ \Delta\bar{p} + \frac{1}{2}(3n + 1)[(1 - \nu^2)\beta](\Delta\bar{p})^2 + \frac{1}{6}(3n + 1)(3n + 2)[(1 - \nu^2)\beta]^2(\Delta\bar{p})^3 + \mathcal{O}(\beta^3) \right\}. \quad (\text{C7})$$

On the other hand, a Taylor series expansion of Eq. (5.8) leads to

$$\bar{q}^n = \frac{1}{2(3 + 1/n)^n} \left\{ \Delta\bar{p} + \frac{1}{2}(3n + 1)[(1 - \nu^2)\beta](\Delta\bar{p})^2 + \frac{1}{6}(3n)(3n + 1)[(1 - \nu^2)\beta]^2(\Delta\bar{p})^3 + \mathcal{O}(\beta^3) \right\}. \quad (\text{C8})$$

Equations (C7) and (C8) agree to *two terms*, with the first discrepancy being the relatively minor change of  $3n$  becoming  $3n + 1$  in the coefficient of  $(\Delta\bar{p})^3$ .

Now, writing Eq. (C6) in dimensional variables and specializing it to Newtonian fluids ( $n = 1$ ,  $m = \mu$ ), we obtain

$$\frac{\mu q \ell}{\pi a^4} = \frac{Et}{24(1 - \nu^2)a} \left\{ \left[ 1 - \frac{(1 - \nu^2)a}{Et} \Delta p \right]^{-3} - 1 \right\}. \quad (\text{C9})$$

Equation (C9) can be compared to the corresponding flow rate–pressure drop relation from Fung’s textbook (Fung 1997, §3.4, Eq. (8)):

$$\frac{\mu q \ell}{\pi a^4} = \frac{Et}{24a} \left\{ \left[ 1 - \frac{a}{Et} \Delta p \right]^{-3} - 1 \right\}. \quad (\text{C10})$$

Clearly, Eqs. (C9) and (C10) are quite similar with Eq. (C10) simply being the case

of  $\nu = 0$  of Eq. (C9). The physical reason for this mathematical fact is that, in Fung's analysis, the cylinder's axial stresses and deformation are neglected (yielding a state of *uniaxial* stress), which means that Fung's result is a so-called *independent-ring model*. This approximation is distinct from the models derived herein, in which the shell is in a *plane* stress configuration (i.e., both  $\sigma_{\theta\theta}$  and  $\sigma_{zz}$  are taken into account). Therefore, Fung's result, being independent of the Poisson ratio, is strictly applicable only to highly compressible solids such as cork, rather than rubber-like elastomers such as PDMS microtubes or blood vessels. Finally, it is easy to show that Eqs. (C9) and (C10) both reduce to Poiseuille's law by performing a Taylor series expansion in  $\Delta p \ll Et/a$  and keeping only the leading-order term. The first difference between the two expressions arises at  $\mathcal{O}([a\Delta p/(Et)]^2)$ , in which the factor of  $(1 - \nu^2)$  comes up. Therefore, for small and moderate  $\Delta p$  (compared to  $Et/a$ ), Fung's result will, perhaps *a priori* unexpectedly, produce an acceptable approximation of the pressure drop in a deformable tube.

## REFERENCES

- ABGRALL, P. & GUÉ, A. M. 2007 Lab-on-chip technologies: making a microfluidic network and coupling it into a complete microsystema review. *J. Micromech. Microeng.* **17**, R15.
- ANAND, V. & CHRISTOV, I. C. 2019 On the Deformation of a Hyperelastic Tube Due to Steady Viscous Flow Within. In *Dynamical Processes in Generalized Continua and Structures* (ed. H. Altenbach, A. Belyaev, V. A. Eremeyev, A. Krivtsov & Porubov. A. V.), *Springer Series on Advanced Structured Materials*, vol. 103, chap. 2, pp. 17–35. Cham, Switzerland: Springer Nature.
- ANAND, V., DAVID JR, J. & CHRISTOV, I. C. 2019 Non-Newtonian fluid–structure interactions: Static response of a microchannel due to internal flow of a power-law fluid. *J. Non-Newtonian Fluid Mech.* **264**, 62–72.
- ANSYS INC. 2018 ANSYS® Academic Research Mechanical, Release 19.0 Help System, Coupled Field Analysis Guide, ANSYS, Inc. *Tech. Rep.*.
- AUROUX, P.-A., IOSSIFIDIS, D., REYES, D. R. & MANZ, A. 2002 Micro total analysis systems. 2. Analytical standard operations and applications. *Anal. Chem.* **74**, 2637–2652.
- AUTON, L. C. & MACMINN, C. W. 2017 From arteries to boreholes: steady-state response of a poroelastic cylinder to fluid injection. *Proc. R. Soc. A* **473**, 20160753.
- AYYASWAMY, P. S. 2016 Introduction to Biofluid Mechanics. In *Fluid Mechanics*, 6th edn. (ed. P. K. Kundu, I. M. Cohen & D. R. Dowling), chap. 16, pp. e1–e73. San Diego, CA: Academic Press, an imprint of Elsevier Inc.
- BALMFORTH, N. J., FRIGAARD, I. A. & OVARLEZ, G. 2014 Yielding to stress: Recent developments in viscoplastic fluid mechanics. *Annu. Rev. Fluid Mech.* **46**, 121–146.
- BAZILEVS, Y., TAKIZAWA, K. & TEZDUYAR, T. E. 2013 *Computational Fluid-Structure Interaction Methods and Applications*. Chichester, UK: John Wiley & Sons Inc.
- BERTRAM, C. D. & PEDLEY, T. J. 1982 A mathematical model of unsteady collapsible tube behaviour. *J. Biomech.* **15**, 39–50.
- BIRD, R. B. 1976 Useful non-Newtonian models. *Annu. Rev. Fluid Mech.* **8**, 13–34.
- BIRD, R. B., ARMSTRONG, R. C. & HASSAGER, O. 1987 *Dynamics of Polymeric Liquids*, 2nd edn., , vol. 1. New York: John Wiley.
- BOYKO, E., BERCOVICI, M. & GAT, A. D. 2017 Viscous-elastic dynamics of power-law fluids within an elastic cylinder. *Phys. Rev. Fluids* **2**, 073301.
- BRUUS, H. 2008 *Theoretical Microfluidics*. Oxford, UK: Oxford University Press.
- ČANIĆ, S., GUIDOBONI, G. & MIKELIĆ, A. 2007 Fluid-structure interaction in a pre-stressed tube with thick elastic walls I: the stationary Stokes problem. *Netw. Heterog. Media* **2**, 397–423.
- ČANIĆ, S., HARTLEY, C. J., ROSENSTRAUCH, D., TAMBAČA, J., GUIDOBONI, G. & MIKELIĆ, A. 2006 Blood flow in compliant arteries: An effective viscoelastic reduced model, numerics, and experimental validation. *Ann. Biomed. Eng.* **34**, 575–592.
- ČANIĆ, S. & MIKELIĆ, A. 2003 Effective equations modeling the flow of a viscous incompressible

- fluid through a long elastic tube arising in the study of blood flow through small arteries. *SIAM J. Appl. Dyn. Syst.* **2**, 431–463.
- CHAKRABORTY, D., PRAKASH, J. R., FRIEND, J. & YEO, L. 2012 Fluid-structure interaction in deformable microchannels. *Phys. Fluids* **24**, 102002.
- CHAKRABORTY, S. 2005 Dynamics of capillary flow of blood into a microfluidic channel. *Lab Chip* **5**, 421–430.
- CHIEN, S., USAMI, S., TAYLOR, H. M., LUNDBERG, J. L. & GREGERSEN, M. I. 1966 Effects of hematocrit and plasma proteins on human blood rheology at low shear rates. *J. Appl. Physiol.* **21**, 81–87.
- CHOPIN, J., VELLA, D. & BOUDAOU, A. 2008 The liquid blister test. *Proc. R. Soc. A* **464**, 2887–2906.
- CHRISTOV, I. C., COGNET, V., SHIDHORE, T. C. & STONE, H. A. 2018 Flow rate–pressure drop relation for deformable shallow microfluidic channels. *J. Fluid Mech.* **814**, 267–286.
- COSTANZO, F. & BRASSEUR, J. G. 2015 The invalidity of the Laplace law for biological vessels and of estimating elastic modulus from total stress vs. strain: A new practical method. *Math. Med. Biol.* **32**, 1–37.
- CRESPI-LORENS, D., VICENTE, P. & VIEDMA, A. 2015 Generalized Reynolds number and viscosity definitions for non-Newtonian fluid flow in ducts of non-uniform cross-section. *Exp. Thermal Fluid Sci.* **64**, 125–133.
- DAVIS, S. H. 2017 The importance of being thin. *J. Eng. Math.* **105**, 3–30.
- DIXIT, T. & GHOSH, I. 2015 Review of micro- and mini-channel heat sinks and heat exchangers for single phase fluids. *Renew. Sust. Energ. Rev.* **41**, 1298–1311.
- DONNELL, L. H. 1933 Stability of thin-walled tubes under torsion. *Tech. Rep.*. NACA-TR-479.
- DUPRAT, C. & STONE, H. A., ed. 2016 *Fluid–Structure Interactions in Low-Reynolds-Number Flows*. Cambridge, UK: The Royal Society of Chemistry.
- DYM, C. L. 1990 *Introduction to the Theory of Shells*. New York, NY: Hemisphere Publishing Corporation.
- EBRAHIMI, A. P. 2009 Mechanical properties of normal and diseased cerebrovascular system. *J. Vasc. Interv. Neurol.* **2**, 155–162.
- ELBAZ, S. B. & GAT, A. D. 2014 Dynamics of viscous liquid within a closed elastic cylinder subject to external forces with application to soft robotics. *J. Fluid Mech.* **758**, 221–237.
- ELBAZ, S. B. & GAT, A. D. 2016 Axial creeping flow in the gap between a rigid cylinder and a concentric elastic tube. *J. Fluid Mech.* **806**, 580–602.
- ELBAZ, S. B., JACOB, H. & GAT, A. D. 2018 Transient gas flow in elastic microchannels. *J. Fluid Mech.* **846**, 460–481.
- FLÜGGE, W. 1960 *Stresses in Shells*. Berlin/Heidelberg: Springer.
- FUNG, Y. C. 1993 *Biomechanics: Mechanical Properties of Living Tissues*. New York, NY: Springer-Verlag.
- FUNG, Y. C. 1997 *Biomechanics: Circulation*, 2nd edn. New York, NY: Springer-Verlag.
- GAY-BALMAZ, F., GEORGIEVSKII, D. & PUTKARADZE, V. 2018 Stability of helical tubes conveying fluid. *J. Fluids Struct.* **78**, 146–174.
- GERVAIS, T., EL-ALI, J., GÜNTHER, A. & JENSEN, K. F. 2006 Flow-induced deformation of shallow microfluidic channels. *Lab Chip* **6**, 500–507.
- GROTBERG, J. B. 1994 Pulmonary Flow and Transport Phenomena. *Annual Review of Fluid Mechanics* **26** (1), 529–571.
- GROTBERG, J. B. & JENSEN, O. E. 2004 Biofluid mechanics in flexible tubes. *Annu. Rev. Fluid Mech.* **36**, 121–147.
- HAPPEL, J R & BRENNER, H 1983 *Low Reynolds Number Hydrodynamics*, 2nd edn. The Hague: Martinus Nijhoff Publishers.
- HARDY, B. S., UECHI, K., ZHEN, J. & PIROUZ KAVEHPOUR, H. 2009 The deformation of flexible PDMS microchannels under a pressure driven flow. *Lab Chip* **9**, 935–938.
- HEIL, M. 1997 Stokes flow in collapsible tubes: computation and experiment. *J. Fluid Mech.* **353**, 285–312.
- HEIL, M. & HAZEL, A. L. 2011 Fluid-structure interaction in internal physiological flows. *Annu. Rev. Fluid Mech.* **43**, 141–162.
- HEWITT, I. J., BALMFORTH, N. J. & DE BRUYN, J. R. 2015 Elastic-plated gravity currents. *Eur. J. Appl. Math.* **26**, 1–31.

- HOLMES, M. H. 2013 *Introduction to Perturbation Methods, Texts in Applied Mathematics*, vol. 20. New York, NY: Springer Science+Business Media.
- HUSSAIN, M. A., KAR, S. & PUNIYANI, R. R. 1999 Relationship between power law coefficients and major blood constituents affecting the whole blood viscosity. *J. Biosci.* **24**, 329–337.
- JONES, E., OLIPHANT, T., PETERSON, P. & OTHERS 2001 SciPy: Open source scientific tools for Python. GitHub.
- JUEL, A., PIHLER-PUZOVIĆ, D. & HEIL, M. 2018 Instabilities in blistering. *Annu. Rev. Fluid Mech.* **50**, 691–714.
- KANG, C. K., ROH, C. H. & OVERFELT, R. A. 2014 Pressure-driven deformation with soft polydimethylsiloxane (PDMS) by a regular syringe pump: challenge to the classical fluid dynamics by comparison of experimental and theoretical results. *RSC Adv.* **4**, 3102–3112.
- KARAN, P., CHAKRABORTY, J. & CHAKRABORTY, S. 2018 Small-scale flow with deformable boundaries. *J. Indian Inst. Sci.* **98**, 159–183.
- KELLER, H. B. 1976 *Numerical Solution of Two Point Boundary Value Problems, CBMS-NSF Regional Conference Series in Applied Mathematics*, vol. 24. Philadelphia, PA: SIAM.
- KITSON, P. J., ROSNES, M. H., SANS, V., DRAGONE, V. & CRONIN, L. 2012 Configurable 3D-Printed millifluidic and microfluidic ‘lab on a chip’ reactionware devices. *Lab Chip* **12**, 3267–3271.
- KIZILOVA, N., HAMADICHE, M. & GAD-EL HAK, M. 2012 Mathematical models of biofluid flows in compliant ducts. *Arch. Mech.* **64**, 65–94.
- KLEINSTREUER, C. 2006 *Biofluid Dynamics: Principles and Selected Applications*. Boca Raton, FL: CRC Press, an imprint of Taylor & Francis Group.
- KONG, L. X., PEREBIKOVSKY, A., MOEBIUS, J., KULINSKY, L. & MADOU, M. 2016 Lab-on-a-CD. *J. Lab. Automat.* **21**, 323–355.
- KRAUS, H. 1967 *Thin Elastic Shells*. New York, NY: John Wiley & Sons.
- LAUGA, E. 2016 Bacterial hydrodynamics. *Annu. Rev. Fluid Mech.* **48**, 105–130.
- LEAL, L. G. 2007 *Advanced Transport Phenomena: Fluid Mechanics and Convective Transport Processes*. New York, NY: Cambridge University Press.
- LEE, L. J. 2006 BioMEMS. In *Encyclopedia of Chemical Processing* (ed. S. Lee), , vol. 1, pp. 161–169. New York: Taylor & Francis.
- LOVE, A E H 1888 The small free vibrations and deformation of a thin elastic shell. *Phil. Trans. R. Soc. Lond. A* **179**, 491–546.
- MADOU, M., ZOVAL, J., JIA, G., KIDO, H., KIM, J. & KIM, N. 2006 Lab on a CD. *Annu. Rev. Biomed. Eng.* **8**, 601–628.
- MATSUMOTO, T., SUGITA, S. & YAGUCHI, T. 2015 Biomechanics of blood vessels: Structure, mechanics, and adaptation. In *Advances in Metallic Biomaterials, Springer Series in Biomaterials Science and Engineering*, vol. 3, chap. 4, pp. 71–98. Berlin/Heidelberg: Springer-Verlag.
- MINDLIN, R. D. 1951 Influence of rotatory inertia and shear on flexural motions of isotropic, elastic plates. *ASME J. Appl. Mech.* **18**, 31–38.
- NAGRATH, S., SEQUIST, L. V., MAHESWARAN, S., BELL, D. W., IRIMIA, D., ULKUS, L., SMITH, M. R., KWAK, E. L., DIGUMARTHY, S., MUZIKANSKY, A., RYAN, P., BALIS, U. J., TOMPKINS, R. G., HABER, D. A. & TONER, M. 2007 Isolation of rare circulating tumour cells in cancer patients by microchip technology. *Nature* **450**, 1235–1239.
- NEU, J. C. 2015 *Singular Perturbation in the Physical Sciences, Graduate Studies in Mathematics*, vol. 167. Providence, RI: American Mathematical Society.
- NGUYEN, N.-T. & WERELEY, S. T. 2006 *Fundamentals and Applications of Microfluidics*, 2nd edn. Norwood, MA: Artech House.
- OLUFSEN, M. S., PESKIN, C. S., KIM, W. Y., PEDERSEN, E. M., NADIM, A. & LARSEN, J. 2000 Numerical simulation and experimental validation of blood flow in arteries with structured-tree outflow conditions. *Ann. Biomed. Eng.* **28**, 1281–1299.
- OZSUN, O., YAKHOT, V. & EKINCI, K. L. 2013 Non-invasive measurement of the pressure distribution in a deformable micro-channel. *J. Fluid Mech.* **734**, R1.
- PAEK, J., CHO, I. & KIM, J. 2015 Microrobotic tentacles with spiral bending capability based on shape-engineered elastomeric microtubes. *Sci. Rep.* **5**, 10768.
- PEDLEY, T. J. 1980 *The Fluid Mechanics of Large Blood Vessels*. Cambridge: Cambridge University Press.

- RAJ, A. & SEN, A. K. 2016 Flow-induced deformation of compliant microchannels and its effect on pressure–flow characteristics. *Microfluid. Nanofluid.* **20**, 31.
- RAJ, M. K., DASGUPTA, S. & CHAKRABORTY, S. 2017 Hydrodynamics in deformable microchannels. *Microfluid. Nanofluid.* **21**, 70.
- RAJ M, K., CHAKRABORTY, J., DASGUPTA, S. & CHAKRABORTY, S. 2018 Flow-induced deformation in a microchannel with a non-Newtonian fluid. *Biomicrofluidics* **12**, 034116.
- REYES, D. R., IOSSIFIDIS, D., AUROUX, P.-A. & MANZ, A. 2002 Micro total analysis systems. 1. Introduction, theory, and technology. *Anal. Chem.* **74**, 2623–2636.
- RUBINOW, S. I. & KELLER, J. B. 1972 Flow of a viscous fluid through an elastic tube with applications to blood flow. *J. Theor. Biol.* **34**, 299–313.
- SAN, O. & STAPLES, A. E. 2012 Dynamics of pulsatile flows through elastic microtubes. *Int. J. Appl. Mech.* **4**, 1250006.
- SANDBERG, L. B., GRAY, W. R. & FRANZBLAU, C., ed. 1977 *Elastin and Elastic Tissue, Advances in Experimental Medicine and Biology*, vol. 79. New York: Plenum Press.
- SEKER, E., LESLIE, D. C., HAJ-HARIRI, H., LANDERS, J. P., UTZ, M. & BEGLEY, M. R. 2009 Nonlinear pressure-flow relationships for passive microfluidic valves. *Lab Chip* **9**, 2691–2697.
- SHAPIRO, A. H. 1977 Steady flow in collapsible tubes. *ASME J. Biomech. Eng.* **99**, 126–147.
- SHIDHORE, T. C. & CHRISTOV, I. C. 2018 Static response of deformable microchannels: a comparative modelling study. *J. Phys.: Condens. Matter* **30**, 054002.
- SQUIRES, T. M. & QUAKE, S. R. 2005 Microfluidics: Fluid physics at the nanoliter scale. *Rev. Mod. Phys.* **77**, 977–1026.
- SU, W., COOK, B. S., FANG, Y. & TENTZERIS, M. M. 2016 Fully inkjet-printed microfluidics: A solution to low-cost rapid three-dimensional microfluidics fabrication with numerous electrical and sensing applications. *Sci. Rep.* **6**, 1–12.
- SUN, J., MASTERMAN-SMITH, M. D., GRAHAM, N. A., JIAO, J., MOTTAHEDEH, J., LAKS, D. R., OHASHI, M., DEJESUS, J., KAMEI, K. I., LEE, K. B., WANG, H., YU, Z.T. F., LU, Y. T., HOU, S., LI, K., LIU, M., ZHANG, N., WANG, S., ANGENIEUX, B., PANOSYAN, E., SAMUELS, E. R., PARK, J., WILLIAMS, D., KONKANKIT, V., NATHANSON, D., VAN DAM, R. M., PHELPS, M. E., WU, H., LIAU, L. M., MISCHEL, P. S., LAZAREFF, J. A., KORNBUM, H. I., YONG, W. H., GRAEBER, T. G. & TSENG, H. R. 2010 A microfluidic platform for systems pathology: Multiparameter single-cell signaling measurements of clinical brain tumor specimens. *Cancer Res.* **70**, 6128–6138.
- SUTERA, S. P. & SKALAK, R. 1993 The history of Poiseuille’s Law. *Annu. Rev. Fluid Mech.* **25**, 1–19.
- TAVAKOL, B., FROEHLICHER, G., STONE, H. A. & HOLMES, D. P. 2017 Extended lubrication theory: Improved estimates of flow in channels with variable geometry. *Proc. R. Soc. A* **473**, 20170234.
- TIMOSHENKO, S. & WOINOWSKY-KRIEGER, S. 1959 *Theory of Plates and Shells*, 2nd edn. New York: McGraw-Hill.
- VLACHOPOULOS, C., O’ROURKE, M. & NICHOLS, W. W. 2011 *McDonald’s Blood Flow in Arteries: Theoretical, Experimental and Clinical Principles*. Boca Raton, FL: CRC Press.
- WAGNER, N. J. & BRADY, J. F. 2009 Shear thickening in colloidal dispersions. *Phys. Today* **62** (10), 27–32.
- WEISBERG, A., BAU, H. H. & ZEMEL, J. N. 1992 Analysis of microchannels for integrated cooling. *Int. J. Heat Mass Transfer* **35**, 2465–2474.
- WHITESIDES, G. M. 2006 The origins and the future of microfluidics. *Nature* **442**, 368–373.
- WHITTAKER, R. J., HEIL, M., JENSEN, O. E. & WATERS, S. L. 2010 A rational derivation of a tube law from shell theory. *Q. J. Mech. Appl. Math.* **63**, 465–496.
- WU, F., CHEN, S., CHEN, B., WANG, M., MIN, L., ALVARENGA, J., JU, J., KHADEMOSSEINI, A., YAO, Y., ZHANG, Y. S., AIZENBERG, J. & HOU, X. 2018 Bioinspired universal flexible elastomer-based microchannels. *Small* **14**, 1702170.
- XIA, Y. & WHITESIDES, G. M. 1998 Soft lithography. *Annu. Rev. Mater. Sci.* **28**, 153–184.